Complex Phase Formation in Particle-Forming AB/AB' Diblock Copolymer Blends with Variable Core Block Lengths

Aaron P. Lindsay, Guo Kang Cheong, Austin J. Peterson, Steven Weigand, Kevin D. Dorfman, Timothy P. Lodge, Prank S. Bates*, Bates*,

¹Department of Chemical Engineering and Materials Science and ²Department of Chemistry, University of Minnesota, Minneapolis, MN 55455, USA

³DND-CAT Synchrotron Research Center, Northwestern University, APS/ANL Building 432-A004, 9700 South Cass Avenue, Argonne, IL 60439, USA

KEYWORDS. Diblock copolymer blends, Frank–Kasper phases, quasicrystals, X-ray scattering

ABSTRACT. Over the past decade, a wealth of complexity has been reported in the packing of compositionally asymmetric, particle-forming diblock copolymer melts, beginning with the discovery of the Frank-Kasper of phase and continuing with subsequent discoveries of a dodecagonal quasicrystal and the C14, C15, and A15 phases. First identified by self-consistent field theory (SCFT), blending diblock copolymers has proven to be a useful strategy in extending these packings to new chemistries and length scales. However, much of the immense phase space created on blending two copolymers remains unexplored. Herein, we expand on our past work investigating binary blends of polystyrene-block-1,4-polybutadiene (SB) diblock copolymers, focusing on binary mixtures with a constant corona (majority) block length and a range of ratios of core (minority) block lengths. Small-angle X-ray scattering and transmission electron microscopy conducted with 5 narrow dispersity diblock copolymers and the associated blends uncovered a rich phase space including 12 distinct nanostructures. Notably, in agreement with SCFT predictions, we document a C14 Laves phase at low fractions of the larger copolymer in a mixture of high and low molecular weight components. However, experiments and SCFT calculations reveal that this window is truncated by close packing when the smaller copolymer is weakly segregated. Moreover, we find that even a modest difference in core block lengths is sufficient to stabilize the σ phase, highlighting the impact of core block dispersity in past studies as well as the utility of blending in accessing these complex particle phases.

INTRODUCTION

AB-diblock copolymers self-assemble into an array of interesting nanostructures, largely as a function of the composition $f_i = N_i/N$ and segregation strength γN , where N is the number-average degree of polymerization, i denotes block A or B, and χ is the Flory-Huggins parameter.¹ These nanostructures range from lamellae (LAM) in the symmetric case (i.e., $f_i = 0.5$) to network structures, cylinders, and spheres with increasing compositional asymmetry (i.e., $f_i \rightarrow 0$ or $f_i \rightarrow 1$). With the exception of the double gyroid² (GYR) and $Fddd^{3,4}$ network structures identified in the 1990s and early 2000s, respectively, this phase progression has been largely understood since the 1960s, reinforced by the advent of self-consistent mean-field theory^{1,5-9} (SCFT) and extensive studies using a wide range of polymer chemistries. 10-12 However, a renewed focus over the past two decades on the packing of nominally sphere-forming diblock copolymer melts has revealed a wealth of previously unanticipated complexity. In addition to the body-centered cubic (BCC) structure predicted by Leibler¹ and subsequently verified experimentally by Bates and coworkers in the early 1980s, 13 recent work has identified close-packed structures near the order-disorder transition (ODT)^{14,15} as well as several complex Frank–Kasper (FK) phases^{16–19} and an associated dodecagonal quasicrystal (QC).²⁰ These discoveries mirror findings in self-assembled multiblock polymers, ^{17,21–23} star polymers, ^{24,25} lyotropic liquid crystals, ^{26–28} dendrimers, ^{29–31} and giant shape amphiphiles, 32-36 along with seemingly unrelated systems such as metal alloys, 37 clathrates, 38,39 foams, 40-42 and even simple organic salts. 43 Diblock copolymers combine synthetic versatility with theoretical simplicity, offering attractive opportunities to explore universalities underlying phase selection across ostensibly disparate fields in condensed matter physics.

Of particular interest are the FK phases, which exhibit large unit cells (e.g., 30 particles per σ phase unit cell), potentially enabling access to photonic crystals at more modest molecular weights

than is possible with traditional diblock copolymer nanostructures.^{17,44,45} These phases are topologically (or tetrahedrally) close-packed (TCP), meaning that all interstitial sites are tetrahedral.^{46–48} This requires the presence of multiple particle volumes characterized by 12-, 14-, 15-, or 16-fold coordination, which differs from classical close-packed face-centered cubic (FCC) and hexagonally close-packed (HCP) structures, wherein both tetrahedral and the less dense octahedral interstices are present. Critically, above (χN)_{ODT}, a repulsive potential disfavoring intermicelle chain overlap drives densely packed micelles to facet in order to fill space at constant segment density.⁴⁹ This results in particles with a geometry reflective of the Wigner-Seitz polyhedron at each lattice site. Accordingly, these polyhedra are more faceted and thus more spherical on average for the FK phases than the truncated octahedron of the BCC phase.⁴⁹ Hence, their emergence in soft matter is largely rationalized as enthalpic in nature, *i.e.*, a minimization of interfacial area.⁵⁰ Nonetheless, the necessity for multiple particle volumes and geometries in FK phases results in significant chain stretching and compression, which is ultimately why the BCC phase, with its unimodal particle size distribution, generally dominates the phase space.⁵⁰

On this foundation, a number of routes to the FK phases have been developed, increasing access to these packings and improving our understanding of why they form. Until recently, the predominant method employed for systems with a single block junction has been to use an amphiphile with high architectural^{29–31,51,52} or conformational asymmetry^{19,53–55} and low molecular weight.⁵⁶ This approach facilitates access to FK phases—the σ and A15 phases in particular—by stabilizing particles at higher core compositions and/or creating a stiffness contrast that imposes the corona geometry onto the core, in both cases driving an increase in interfacial area. This phase behavior can be further expanded through thermal processing, ^{18,55} which can bias the system towards other TCP phases (*i.e.*, the QC, C14, and C15 phases), or by simply blending a diblock

copolymer with homopolymer^{44,57–61} or another diblock copolymer.^{54,62–65} However, the first two cases (*i.e.*, architectural/conformational asymmetry and thermal processing) are somewhat limited in that they work only for a handful of chemistries and length scales. In contrast, blending is simple, can be executed with essentially any block chemistry, and, as will be shown, affords access to every particle packing thus far discovered in diblock copolymers and over a much wider range of length scales. We focus here on furthering the understanding of bidisperse diblock copolymer blends of the type AB/AB', wherein the block chemistry for each diblock copolymer is identical, but the core (B) block lengths are varied.

Guided by past SCFT predictions, we recently reported on the utility of bidisperse polystyreneblock-1,4-polybutadiene (SB) blends in accessing TCP phases, finding σ, A15, and QC packings in blends of symmetric and asymmetric diblock copolymers with near identical corona block lengths ($N_{\rm S}$) and variable core block lengths ($N_{\rm B}$).⁶³ These packings were characterized by large unit cell dimensions, as much as 101 nm for the σ phase, which is more than double that of previously studied single-component diblock copolymer melts. 17-20,54,66 Moreover, this approach afforded access to these phases in a moderately high molecular weight ($M \approx 30 \text{ kg/mol}$) system with modest conformational asymmetry, where FK phases were not observed in the nominally single component materials.⁵⁶ Together, these findings indicated that this rich phase behavior stemmed from the blending strategy rather than the block chemistry, opening avenues to access these phases in more diverse systems and for M > 10 kg/mol. Indeed, Yamamoto and Takagi recently reproduced a nearly identical phase progression in similar blends of polystyrene-blockpoly(methyl acrylate) (SMA) copolymers.⁶⁴ However, these works represent a narrow sampling of an immense phase space, leaving open several questions. Specifically, how different must the core block lengths be to access these phases, and what happens at low fractions of the larger,

symmetric copolymer? In both our work and that of Yamamoto and Takagi, the system was disordered in the latter limit, yet mean-field theory predicts that Laves phases may be favored.⁶⁵

To answer these questions, we synthesized five SB diblock copolymers using anionic polymerization and prepared a series of bidisperse blends of the type SB/SB'. Small-angle X-ray scattering (SAXS) and transmission electron microscopy (TEM) reveal a rich phase space including 8 distinct particle packings: BCC, σ , A15, C14, QC, HCP, FCC, and a non-ergodic liquid-like packing (LLP). As anticipated by SCFT, a Laves C14 phase is documented at low fractions of the larger copolymer for blends with a large variance in the core block lengths. Moreover, we find that FK phases can be stabilized with a relatively small difference in the core block lengths at fixed overall composition, e.g., blending an asymmetric SB copolymer ($f_B = 0.12$) with a cylinder-forming SB copolymer ($f_B = 0.25$) yields the σ phase. Curiously, at an intermediate difference in core block lengths, the FK phase window is truncated by hexagonal scattering symmetry typical of hexagonally packed cylinders (HEX_C), yet TEM reveals the presence of ordered particles (denoted HEX_s). Repeating the experiments over an extended annealing period reveals FCC and HCP phases, suggesting the unusual scattering reflects a heavily faulted closepacked structure rather than particles on the simple hexagonal lattice previously suggested for tetrablock terpolymers.²¹ We rationalize these results in the context of SCFT as a consequence of an expanded particle phase window (i.e., the sphere-cylinder OOT is pushed to higher compositions with increasing difference in the core block lengths) and differential segregation of the two copolymers within the adopted nanostructures.

MATERIALS AND METHODS

Synthesis. SB diblock copolymers were synthesized by anionic polymerization. A detailed description of the synthesis can be found elsewhere.⁶⁷ Briefly, styrene was purified over di-*n*-butyl

Table 1. Molecular characteristics

Polymer ID	M _n ^a (kg/mol) (¹ H NMR/SEC)	$f_{ m B}{}^{ m b}$	$M_{ m n,S}^{ m c}$ (kg/mol)	$M_{ m n,B}^{ m c}$ (kg/mol)	${\cal D}^{ m d}$	N^{e}	$T_{g,S}^{f}(^{\circ}C)$
SB1	39/41	0.18	33	5.9	1.01	571	99
SB2	59/61	0.53	31	28	1.03	913	99
SB3	28/30	0.12	25	3.0	1.01	401	73
SB4	31/32	0.25	24	6.8	1.01	449	90
SB5	37/35	0.39	24	13	1.02	563	94

^aNumber-average molecular weight determined from proton nuclear magnetic resonance spectroscopy (¹H NMR) via end-group analysis and from size exclusion chromatography (SEC) in tetrahydrofuran (THF) with light scattering detection; results are within the error of the measurements (\pm 10%). ^bVolume fraction of PB calculated from ¹H NMR spectroscopy based on reported densities for PS and 1,4-PB at 140 °C ($\rho_S = 0.996 \text{ g/cm}^3$; $\rho_B = 0.826 \text{ g/cm}^3$) [70,71]; error is estimated to be \pm 0.01. ^cBlock molecular weights determined from ¹H NMR via end-group analysis. ^dMolecular weight dispersity determined from SEC in THF with light scattering detection as $D = M_w/M_n$, where M_w is the weight-average molecular weight. ^eNumber-average degree of polymerization calculated from ¹H NMR data as $N = (M_{n,S} \rho_S^{-1} + M_{n,B} \rho_B^{-1}) N_{av}^{-1} v_{ref}^{-1}$ where N_{av} is Avogadro's number and $v_{ref} = 118 \text{ Å}^3$ is the reference volume. ^fPS glass transition temperature (T_g) determined via differential scanning calorimetry (DSC).

magnesium and initiated in anhydrous cyclohexane under argon with *sec*-butyl lithium. After 4 h, 1,3-butadiene, purified over *n*-butyl lithium, was added and allowed to react for 4 h. The reaction was then terminated with methanol, after which the resulting polymer was precipitated dropwise in a large excess of methanol and dried under vacuum. All reagents were purchased from Sigma Aldrich.

Molecular Characteristics. All polymers were characterized by proton nuclear magnetic resonance spectroscopy (1 H NMR), size exclusion chromatography (SEC), and differential scanning calorimetry (DSC). Molecular characteristics for each of the copolymers can be found in Table 1. 1 H NMR spectra were collected in deuterated chloroform using a Bruker AVANCE HD 500 spectrometer. The number-average molecular weight (M_n) and composition (f_B) were determined from NMR data as described in our past work. 63 Molar mass dispersity and molecular

weight were determined using an Agilent 1260 Infinity liquid chromatograph system equipped with a Wyatt DAWN Heleos II 18-angle light scattering detector and a Wyatt OPTILAB T-rEX refractive index detector (Figure S1); tetrahydrofuran was used as the mobile phase. The refractive index increment $(\partial n/\partial c)$ was taken as the weight average of the homopolymer refractive index increments (*i.e.*, $(\partial n/\partial c)_{PS} = 0.187$ mL/g and $(\partial n/\partial c)_{PB} = 0.130$ mL/g).^{68,69} Small shoulders indicative of coupling and/or early termination were observed in some polymers, but integration revealed the fraction to be negligible (<5 wt.%). Hence, we do not anticipate this to have an appreciable impact on the phase behavior. DSC measurements were collected on a TA Instruments Q1000 DSC using a ramp rate of 10 °C/min. Peaks in the derivative heat flow collected on the second heating cycle were taken as the glass transition temperatures (T_g 's).

Blend Preparation. Bidisperse blends were prepared by co-dissolution in benzene with < 0.1 wt.% butylated hydroxytoluene (BHT) as an antioxidant and freeze-dried under high vacuum; BHT was found in our previous study to have no impact on the phase behavior but delayed the onset of degradation. For all blend sets, the subscripts 1 and 2 will refer to the lower and higher composition copolymer, respectively, ϕ_i will refer to the volume fraction of copolymer 1 or 2, and $\langle f_B \rangle$ will denote the total 1,4-polybutadiene volume fraction in the blend. Volume fractions were calculated as $\phi_i = (m_i/\rho_i) / [(m_1/\rho_1) + (m_2/\rho_2)]$ and $\langle f_B \rangle = \phi_1 f_{B,1} + \phi_2 f_{B,2}$, where m_i is the mass of copolymer i in the blend and ρ_i is its density, determined from homopolymer densities at 140 °C $\langle \rho_S = 0.996 \text{ g/cm}^3; \rho_B = 0.826 \text{ g/cm}^3 \rangle$. To $\gamma_i = 0.996 \text{ g/cm}^3$; $\gamma_i = 0.826 \text{ g/cm}^3 \rangle$.

Small-Angle X-Ray Scattering. Small-angle X-ray scattering (SAXS) experiments were performed at Sectors 5-ID-D and 12-ID-B of the Advanced Photon Source (APS) located at Argonne National Laboratory. 2D scattering data was azimuthally integrated to produce 1D scattering traces with the scattering wavevector $q = 4\pi\lambda^{-1}\sin(\theta/2)$ calibrated using a Au-coated Si

diffraction grating with 7200 lines/mm or silver behenate; θ is the scattering angle and λ is the wavelength of the incident beam. Samples were hermetically sealed under argon in Tzero DSC pans (DSC Consumables) and pre-annealed at various temperatures using hotplates ($T \pm 5$ °C) for times specified in the main text; sealing samples under argon significantly delayed the onset of thermal degradation.⁶³ Samples were then vitrified in liquid nitrogen, transferred to the beamline, and measured at specified temperatures using a custom array heating stage ($T \pm 2$ °C) following 10-30 min of thermal equilibration.

Transmission Electron Microscopy (TEM). Following SAXS measurements, select samples were vitrified with liquid nitrogen, after which thin sections (< 100 nm) were collected at –120 °C using a Leica UC6 microtome. Samples were subsequently vapor-stained with osmium tetroxide (OsO₄) at 50 °C for 30 min; OsO₄ preferentially stains the polybutadiene domains.⁷² Images were then collected using a Tecnai G2 Spirit BioTWIN microscope equipped with a LaB₆ thermionic gun and operated at an accelerating voltage of 120 keV.

Self-Consistent Mean-Field Theory (SCFT). Canonical (*NVT*) and grand-canonical (μVT) SCFT calculations were performed using the open-source Polymer Self-Consistent Field (PSCF) software package⁷³ with combined unit cell and field relaxation.⁷⁴ Calculations were performed in the ϕ_2 – χ (N) phase space for blends with $f_{\rm B,1}=0.12$, $f_{\rm B,2}=0.38$, and $N_2/N_1=1.4$. Conformational asymmetry, calculated as $\varepsilon=(b_{\rm B}/b_{\rm S})^2$ ($v_{\rm S}/v_{\rm B}$) where b is the statistical segment length and v is the segment volume, was chosen to match the experiments ($\varepsilon=1.7$). Canonical SCFT calculations were first performed to assess order–disorder and order–order transitions between candidate phases: DIS, BCC, FCC, HCP, σ , A15, C14, C15, HEXC, and GYR. Grand-canonical ensemble calculations were then leveraged to assess two-phase coexistence between neighboring stable phases.⁷⁵ Further details can be found in the Supporting Information.

RESULTS AND DISCUSSION

Phase Behavior at Low ϕ_2 . To assess the phase behavior at low fractions of the larger, higher composition copolymer ($\phi_2 \rightarrow 0$), we prepared blends of an asymmetric SB copolymer (SB1, $f_B = 0.18$, $M_n = 39$ kg/mol) and a symmetric SB copolymer (SB2, $f_B = 0.53$, $M_n = 59$ kg/mol), illustrated schematically in Figure 1A. Blends were characterized by a roughly equivalent corona block length ($M_{n,S} \approx 32$ kg/mol) and a variable core block length such that the ratio of the overall degrees of polymerization was $N_2/N_1 = 1.6$. These blends are directly comparable to the blends studied in our previous report, 63 with the key difference being the higher molecular weight of the constituent copolymers and the resulting emergence of ordered states at low ϕ_2 . Additional molecular characteristics can be found in Table 1.

As shown in Figure 1A, on cooling SB1 ($\phi_2 = 0$) from 200 °C over the course of 3 days and subsequently reheating to 150 °C at a ~0.3 °C/min ramp rate, we observed distinct scattering reflections at $q/q^* = 1$, $\sqrt{2}$, $\sqrt{3}$... characteristic of the $Im\overline{3}m$ space group symmetry that defines the BCC phase. This window of BCC stability was found to persist at modest loadings of the symmetric copolymer. However, at $\phi_2 = 0.075$, we observed the growth of a dense forest of scattering reflections consistent with the $P6_3/mmc$ space group symmetry of the FK C14 Laves phase (Figures 2 and S2; Table S1). This phase, first observed by Friauf in MgZn₂ alloys, ⁷⁶ is characterized by an (ababab...) stacking of 12-fold coordinated particles interceded by mixed planes of particles with coordination numbers (CN) 12 and 16, wherein the CN16 particles are arranged in a wurtzite structure (Figure 2 inset). ^{48,77,78} Although Laves phases have been anticipated by SCFT for bidisperse blends, ⁶⁵ this represents the first experimental verification of this prediction, adding to the growing list of methods by which these phases can be accessed. ^{18,28,36,59,66}

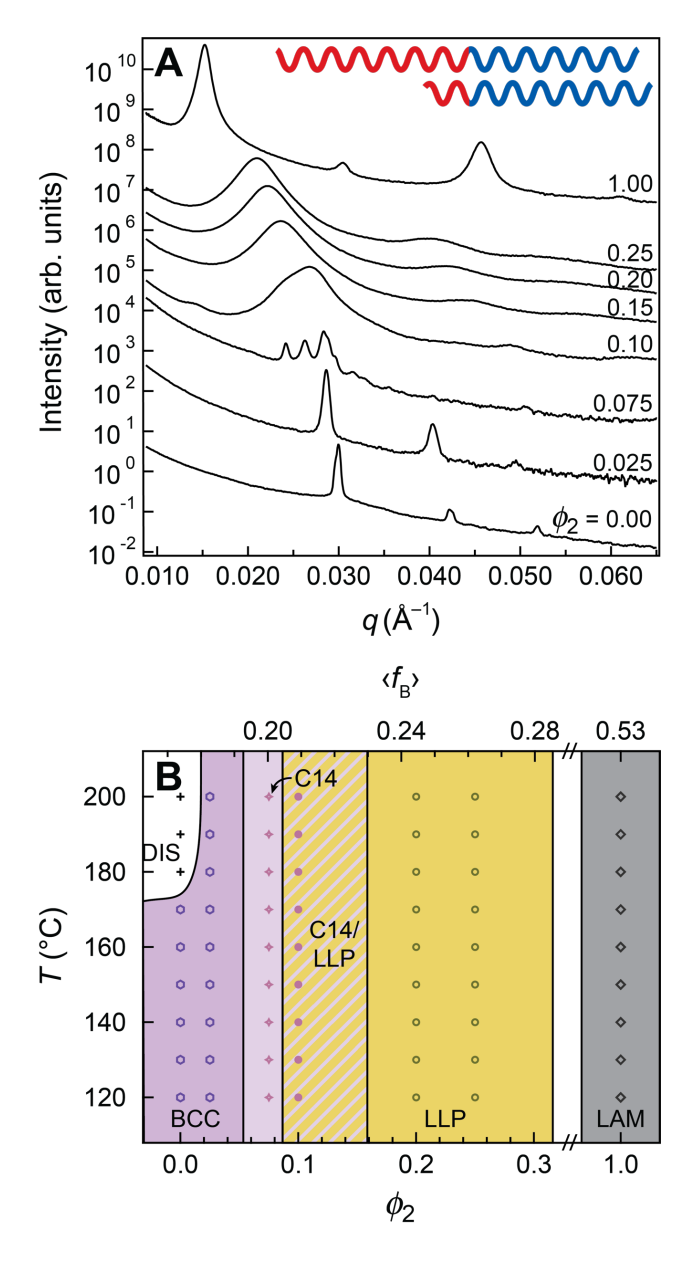


Figure 1. (A) 1D SAXS traces at 150 °C and (B) the associated phase portrait for SB1/SB2 blends. SAXS data were collected on heating approximating a 0.3 °C/min ramp rate following consecutive anneals at 200, 170, and 155 °C for 20, 20, and 24 h, respectively. The schematic in the upper right corner of (A) displays the difference in the relative block lengths for SB1 (bottom) and SB2 (top).

On further increasing the fraction of SB2, the system became kinetically trapped, evidenced by the persistence of a broad scattering reflection well below the ODT, even after extended annealing. At $\phi_2 = 0.10$, there is a shoulder on the principal scattering reflection coupled with a low-q peak at q = 0.0144 Å⁻¹. This peak position is consistent with the anticipated location of the

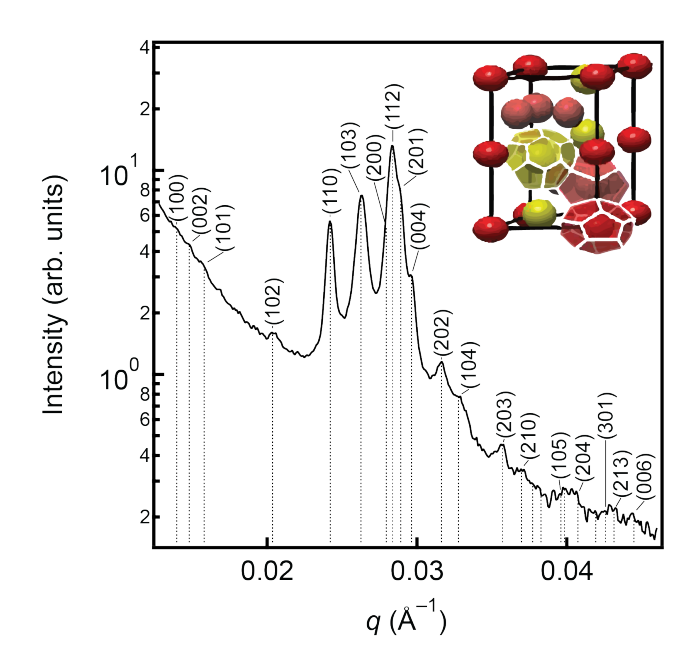


Figure 2. 1D SAXS trace for SB1/SB2 blends with $\phi_2 = 0.075$ at 150 °C indexed to the C14 Laves phase. Inset in upper right corner is a schematic illustration of the C14 Laves phase, where CN12 and CN16 particles are shaded red and yellow, respectively, and representative Wigner–Seitz polyhedra are included for each of the unique Wyckoff positions. SAXS data were collected on heating approximating a 0.3 °C/min ramp rate following consecutive anneals at 200, 170, and 155 °C for 20, 20, and 24 h, respectively.

(100)/(002)/(101) triplet of peaks for the C14 phase or the (111) peak of the C15 phase, suggesting the Laves window persists to this composition. However, for $\phi_2 > 0.10$, samples were kinetically trapped, evidenced by a broad scattering reflection consistent with a liquid-like packing (LLP) that lacks long-range order. In our previous work, we found the ordering time to scale roughly as $t \sim \langle N \rangle^3$ near the ODT, comparable to the *N*-dependence of chain relaxation in an entangled melt.⁶³ However, extensive work on 1,4-polyisoprene-*block*-poly(±-lactide) (IL),^{20,49} in addition to more recent studies on poly(ethylene-*alt*-propylene)-*block*-polydimethylsiloxane⁷⁹ (PEP-PDMS) and dendron-like giant molecules,⁸⁰ have revealed an even more dramatic increase in the ordering time on cooling far below the ODT. At a purported structural glass transition or ergodicity temperature $T_{\rm erg}$, distinct from the molecular level $T_{\rm g}$'s of the constituent blocks, the particle ordering time increases asymptotically, transitioning from mass-exchange-mediated to much slower micelle-translation-mediated ordering kinetics.²⁰ Together, these effects significantly complicate access to

FK phases at high molecular weight, particularly for blends with inaccessible ODTs. We note that a comparable increase in the ordering time is not observed outside the particle phase window. SB2 ordered into LAM following identical annealing protocols and similar investigations of cylinder-forming IL copolymers^{81,82} appear unaffected by $T_{\rm erg}$ of the adjacent particle phase window. Nonetheless, when combined with our previous work on comparable blends at lower molecular weight, it is clear that diblock copolymer blends are useful in generating multiple FK phases including σ , A15, and C14.

Impact of Reducing the Difference in Core Block Lengths. To better understand the limits of this approach, we prepared additional SB/SB' blends. First, we blended the asymmetric copolymer SB3 ($f_B = 0.12$, $M_n = 28$ kg/mol) with the less asymmetric SB4 ($f_B = 0.25$, $M_n = 31$ kg/mol), where $N_2/N_1 = 1.1$. A second set of blends was prepared with SB3 and the modestly off-symmetric SB5 ($f_B = 0.39$, $M_n = 37$ kg/mol) yielding $N_2/N_1 = 1.4$. In both blend sets, the corona block length was held constant ($M_{n,S} \approx 24$ kg/mol) and the core (B) was varied.

As shown in Figure 3A, the scattering trace for SB3 is completely featureless at 150 °C, consistent with a state of disorder in the weak segregation limit. This state persisted on blending SB3 with SB4 for $\phi_2 \le 0.40$. Increasing ϕ_2 to 0.50 and annealing at 150 °C for 169 h resulted in scattering typical of the BCC phase. We attribute the presence of small shoulders in the $\sqrt{2}$ q^* scattering reflections for $\phi_2 = 0.50$ and 0.60 to insufficient re-equilibration at the measurement temperature. Extinction of the $\sqrt{2}$ q^* reflection at $\phi_2 = 0.80$ signals the onset of the HEX_C phase window. Intermediate to the BCC and HEX_C phase windows, the coincidence of $q/q^* = 1$, $\sqrt{3}$, $\sqrt{4}$, $\sqrt{7}$ reflections and a dense array of scattering peaks with $P4_2/mnm$ space group symmetry (Figure 4; Table S2) evidence coexistence of a HEX_C phase and a σ phase with a large unit cell (a = 91.8; c/a = 0.528). Upon heating this sample to 170 °C (Figure 3B), growth of peaks at $\sqrt{2}$ q^* and $\sqrt{5}$ q^* ,

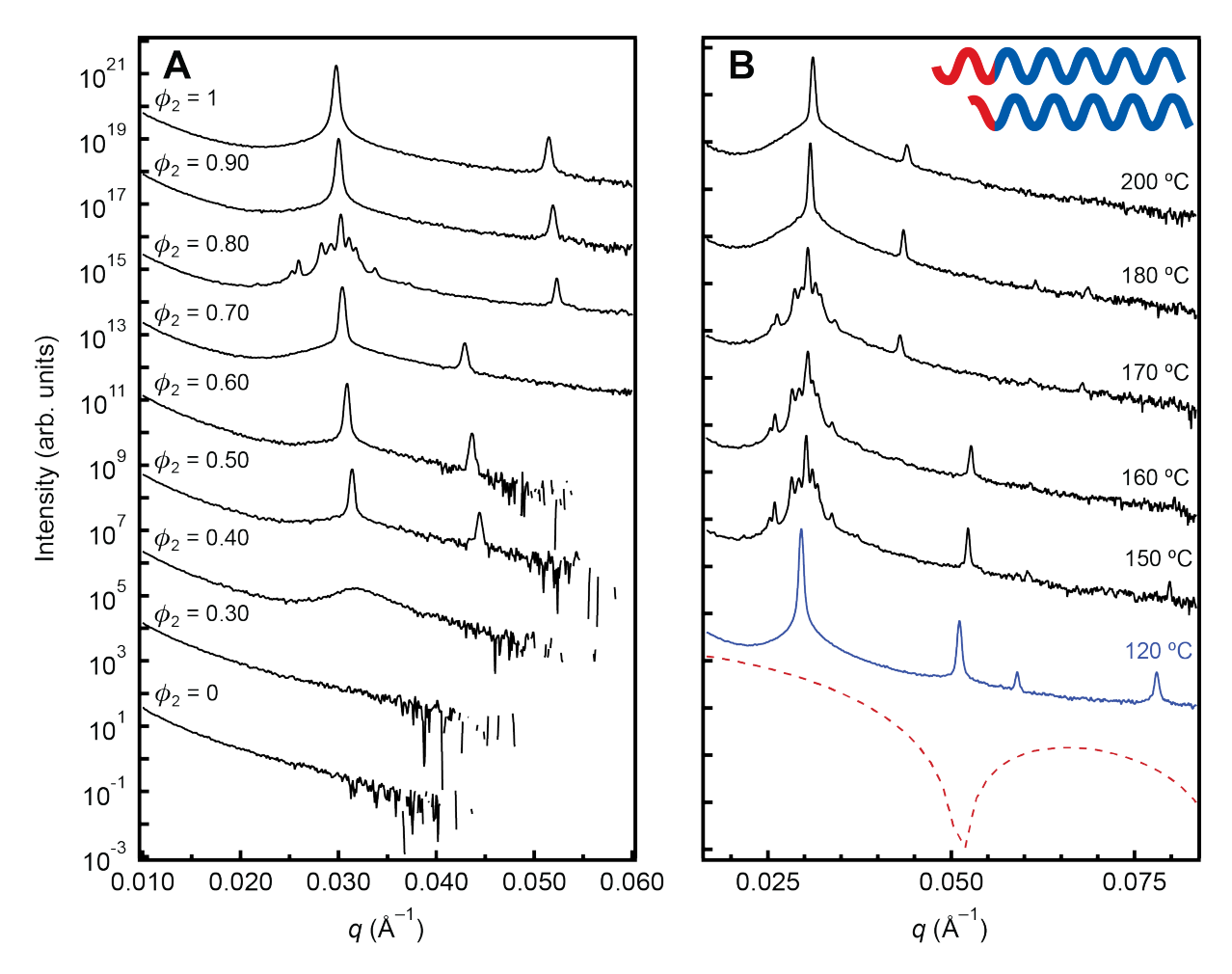


Figure 3. 1D SAXS data collected for SB3/SB4 blends on (A) annealing at 150 °C for 169 h and (B) subsequently heating the sample with $\phi_2 = 0.80$ to 200 °C. The sample was held at each temperature above 150 °C for 5 min. The blue trace in (B) reflects a separate 169 h anneal at 120 °C. The red dashed line corresponds to a spherical form-factor calculated for a core radius of 8.8 nm; this value was determined taking the intense reflection at 0.030 Å⁻¹ as the BCC (110) reflection in the T = 160 °C scattering trace. As can be seen for $T \le 160$ °C, the absence of a $\sqrt{2}$ reflection is indicative of a HEX_C structure and not a form-factor extinction. The schematic in the upper right corner of A displays the difference in the relative block lengths of SB4 (top) and SB3 (bottom).

coupled with an extinction of the $\sqrt{3}$ q^* scattering reflection, signal the onset of σ/BCC phase coexistence; this extinction is consistent with the first minimum of the spherical form-factor (Figure 3B) calculated based on the composition and Bragg reflections for a particle radius $R_{core} = 3^{1/3}2^{1/2}\pi^{2/3} \langle f_{\rm B} \rangle^{1/3} / q_{\rm BCC,110} = 8.8$ nm. Heating further to 180 °C transforms the blend to a virtually pure BCC phase; annealing a sample separately at 180 °C for 169 h showed no evidence of phase coexistence (Figure S3). Similarly, annealing this mixture at 120 °C for 169 h led to a SAXS

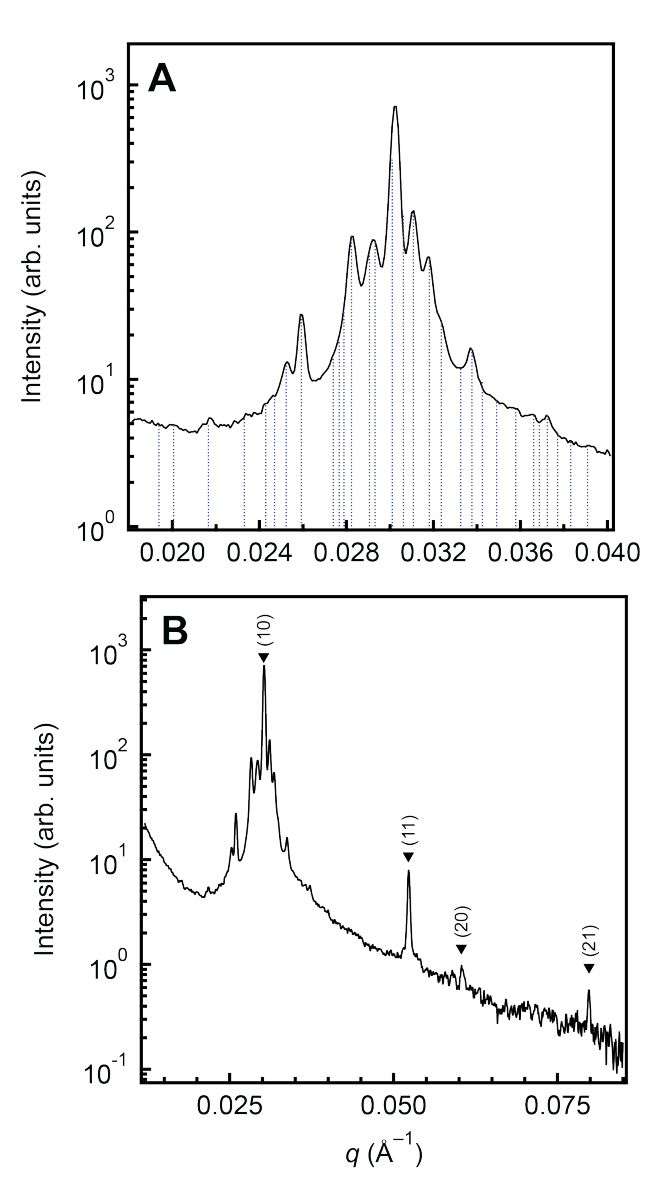


Figure 4. 1D SAXS trace collected from a SB3/SB4 blend with $\phi_2 = 0.80$ and indexed to (A) the σ phase and (B) hexagonally packed cylinders (HEX_C). The sample was annealed at 150 °C for 169 h. Indexing residuals for the σ phase can be found in Table S2.

pattern consistent with a pure HEX_C phase, indicating a HEX_C \rightarrow HEX_C/ σ \rightarrow BCC/ σ \rightarrow BCC phase progression on heating. Although the window of observed σ phase stability is small, our ability to access it with such a modest variation in N_{core} highlights the impact of just a small amount of core block dispersity. We estimate the dispersity of the core block for these blends to be less than 1.2, which we note is likely comparable to that of some previously studied σ -forming isoprene-lactide copolymers (see Supporting Information for further details).

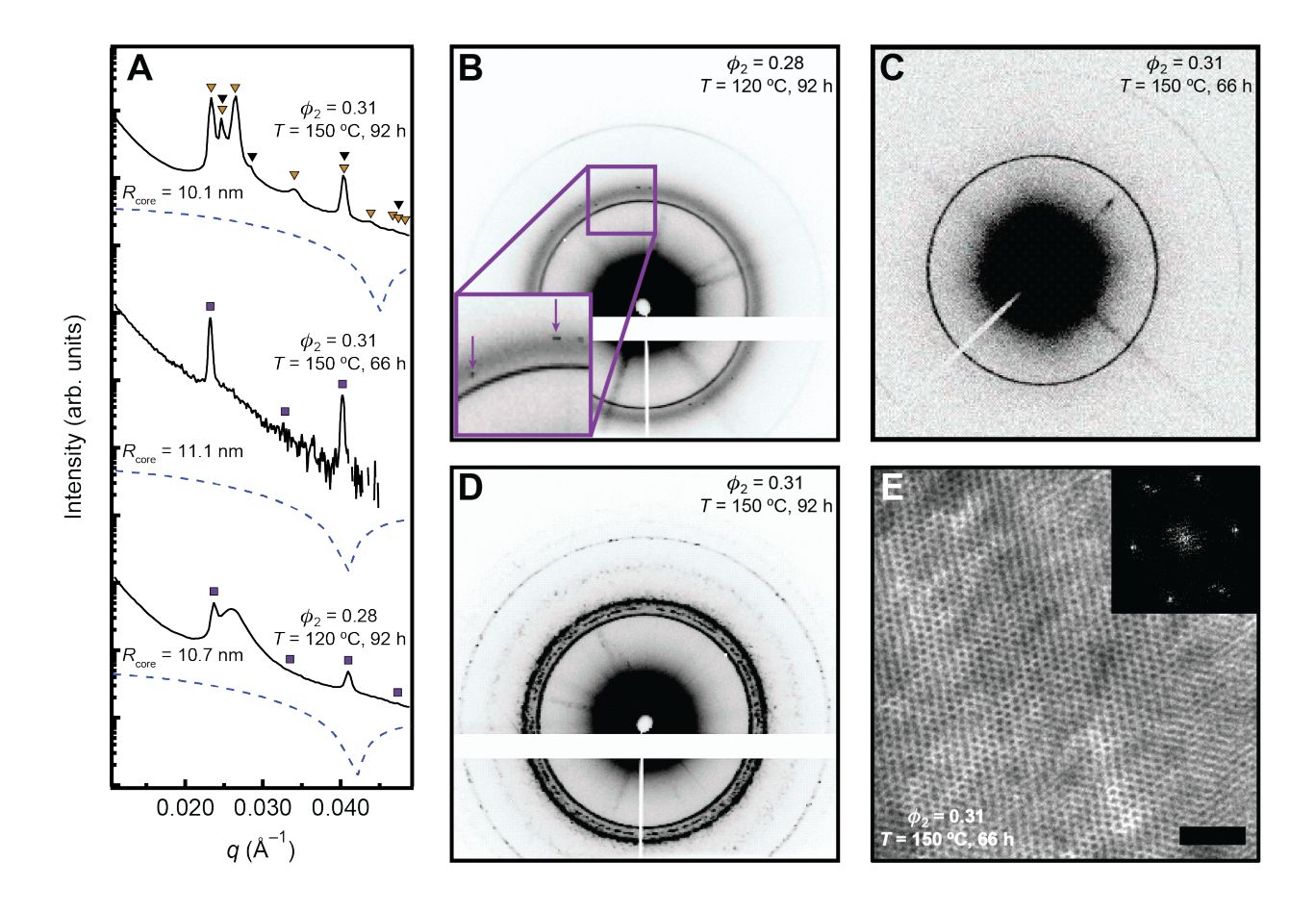


Figure 5. (A-D) SAXS and (E) TEM data collected for SB3/SB5 blends. (A) 1D SAXS traces were obtained by azimuthal integration of 2D SAXS patterns collected from blends with (B) ϕ_2 = 0.28 and (C,D) ϕ_2 = 0.31. Prior to measurement, samples were annealed for (C,E) 66 or (B,D) 92 h at (B) 120 or (C-E) 150 °C. Purple squares, black triangles, and yellow triangles in (A) correspond to a BCC, FCC, or HCP indexing, respectively, and dashed blue lines are spherical form-factors calculated based on the indexed Bragg reflections as described in the text and Supporting Information. The inset in (B) displays a magnified section of the 2D SAXS pattern highlighting spots not captured in the 1D trace. Data for (A,C) SB3/SB5 blends with ϕ_2 = 0.31 after 66 h of annealing was collected at Sector 5-ID-D. The remaining data (A,B,D) were collected at Sector 12-ID-B. The TEM micrograph in (E) was collected from a thin (~70 nm) microtomed section after collecting the SAXS data in (A,C) and vitrifying the sample in liquid nitrogen. The inset in the upper right corner of (E) is a Fourier transform of the image and the scale bar represents 200 nm.

To probe the phase behavior at an intermediate core block length difference, we examined blends of SB3 and SB5, wherein $N_2/N_1 = 1.4$. Similar to the previous blend set, we recorded scattering consistent with disorder for $T \ge 120$ °C and $\phi_2 < 0.28$ (Figure S4A). At $\phi_2 = 0.28$, an unusual

scattering pattern emerged after 92 h of annealing at 120 °C, characterized by sharp, isotropic rings at q^* and $\sqrt{3}$ q^* coupled with a broad ring centered at 1.09 q^* and faint spots at comparable q that were indistinguishable in the 1D trace (Figure 5A,B). The intensity of the broad reflection relative to the sharp Bragg peaks is indicative of the disordered but structured LLP state and peaks at q^* and $\sqrt{3} \ q^*$ could be assigned to a BCC phase based on the composition $\langle f_B \rangle = 0.20$ and relative peak positions. However, as shown in Figure 5A, the lack of a $\sqrt{2} q^*$ reflection cannot be explained by a spherical form factor, which would actually result in extinction of the $\sqrt{3} q^*$ peak. Increasing ϕ_2 further to 0.31 and annealing at 150 °C for 66 h results in a similar scattering pattern but without the broad reflection associated with LLP (Figure 5A,C). Although the sharp, isotropic q^* and $\sqrt{3}$ q^* reflections were observed for scattering patterns collected across the sample, not all patterns displayed spots intermediate to these reflections (Figures 5C and S5). Again, the absence of a $\sqrt{2}$ q^* peak cannot be explained by the associated spherical form factor. This apparent P_6/mm symmetry could point to a HEX_C structure, but, as shown in Figure 4E, we saw no evidence of cylinders on quenching the sample and imaging it by TEM. Rather, we recorded particles ordered with a 6-fold rotational symmetry; a large area (\sim 5 μ m \times 5 μ m) image collected from a different microtomed section yielded the same result (Figure S6).

Zhang *et al.* reported similar scattering in particle-forming polystyrene-*block*-1,4-polyisoprene-*block*-polystyrene-*block*-poly(ethylene oxide) (SISO) tetrablock terpolymers, rationalized as particles on a simple hexagonal lattice (HEX_S) with P_6/mmm space group symmetry and $c/a = \sqrt{3/2}$. For a diblock copolymer, the packing of spheres on a simple hexagonal lattice would require significant chain stretching, owing to the hexagonal prism geometry of the Wigner-Seitz polyhedron. These stretching penalties could presumably be alleviated in our blends by a detachment of one of the copolymers from the core–corona interface; in SISO tetrablock

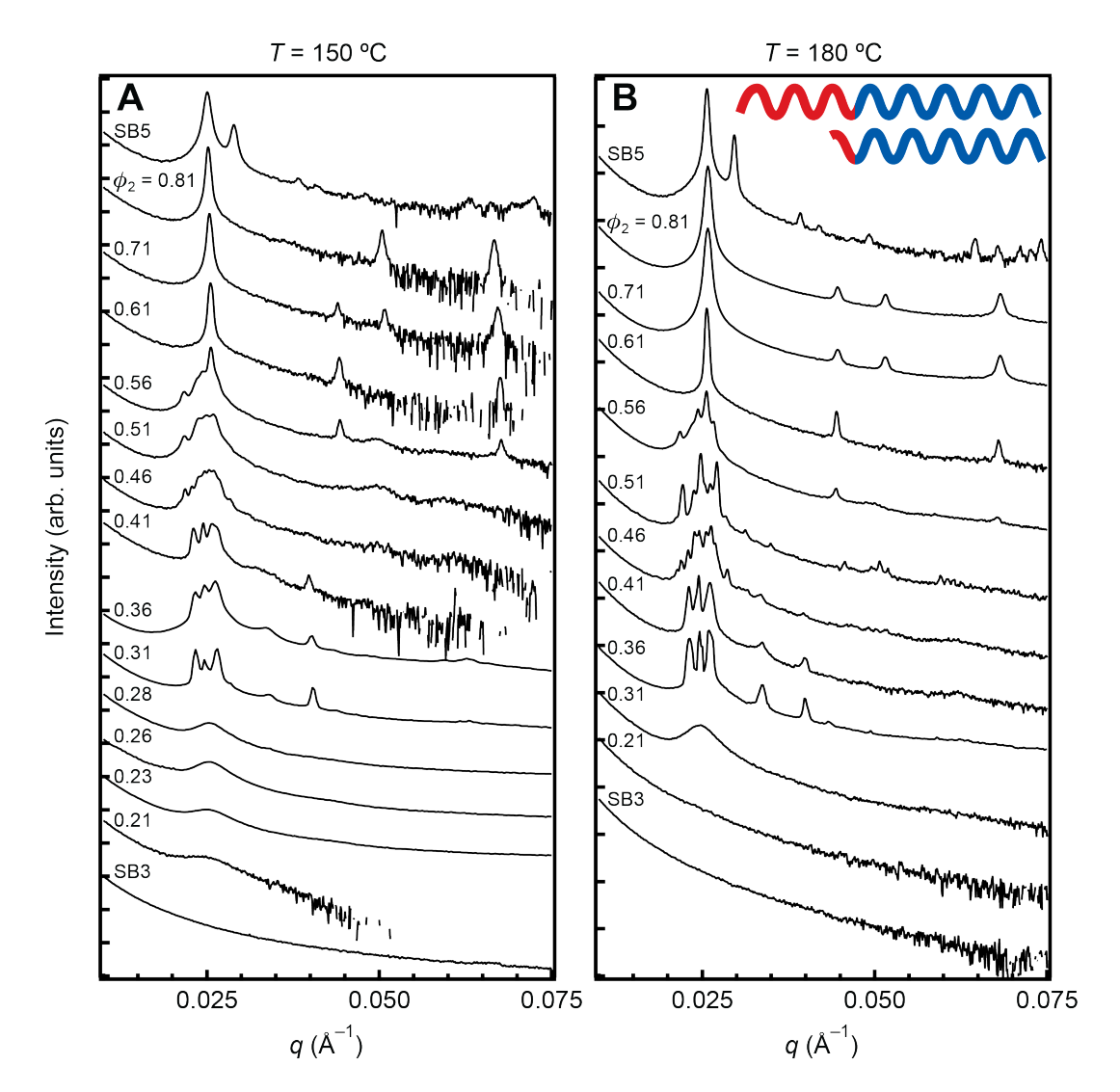


Figure 6. 1D SAXS traces collected from SB3/SB5 blends following extended annealing (66-92 h) at (A) 150 and (B) 180 °C. The schematic in the upper right corner of B displays the difference in the relative block lengths of SB5 (top) and SB3 (bottom).

terpolymers, the emergence of HEX_S was rationalized by a similarly anisotropic distribution of the S and I blocks around the O cores.²¹ However, it is unclear why such a structure would be favored over more classical particle packings such as the BCC, FCC, or HCP phases.

In an effort to better assess the ordered structure at $\phi_2 = 0.31$, we prepared a duplicate sample and annealed it for 92 h. As shown in Figure 5A,D, we obtained a well-resolved HCP/FCC phase coexistence, evidenced by a predominant $P6_3/mmc$ symmetry coupled with a peak at $q/q*_{HCP} = 1.23$ indicative of an added $Fm\overline{3}m$ symmetry; the relative peak intensities and small unit cell

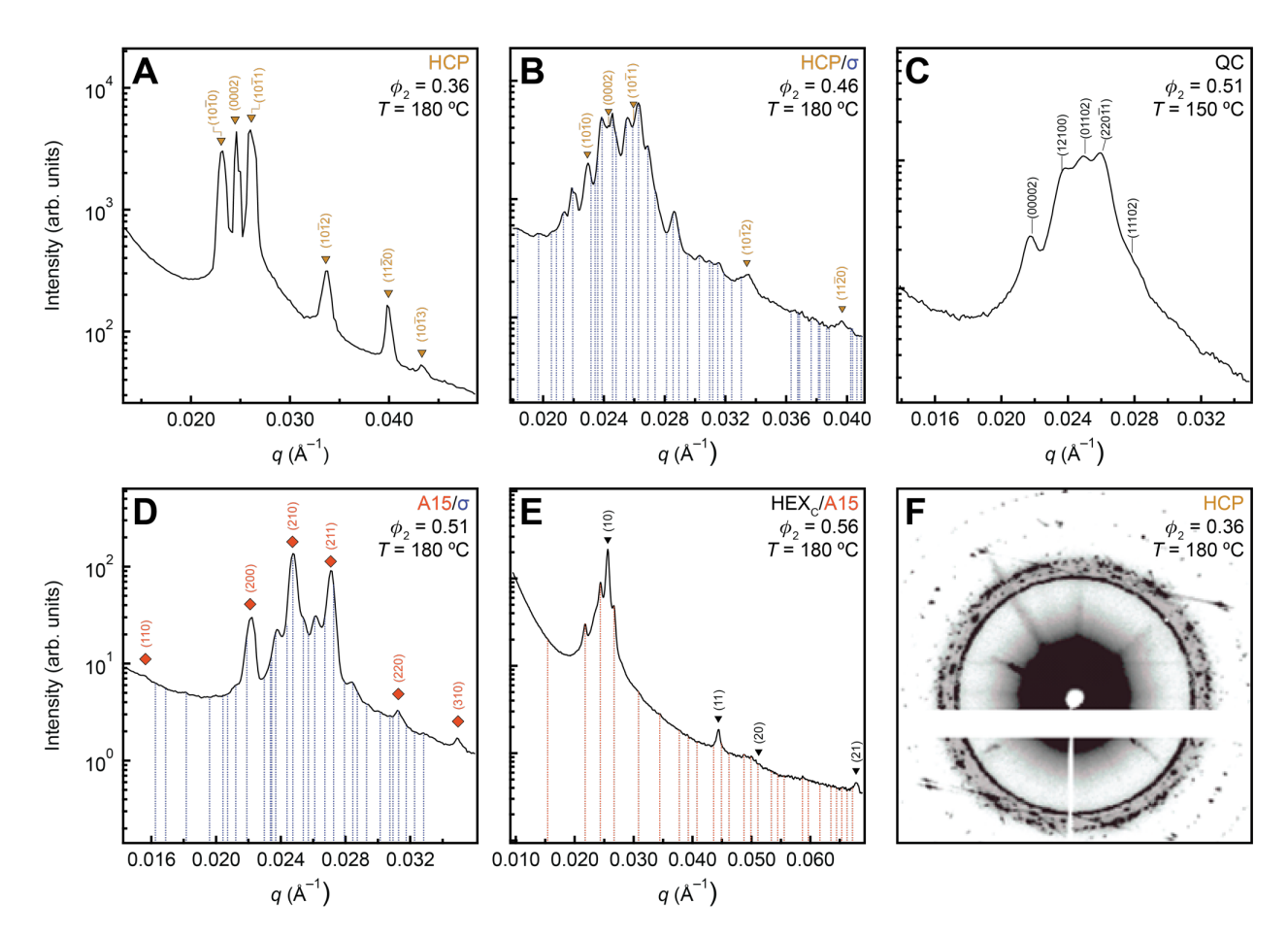


Figure 7. (A-E) 1D and (F) 2D SAXS data collected from SB3/SB5 blends following 66-92 h of annealing at the temperature listed in each panel. Indexing corresponds to the phase(s) listed in each panel and is color coded to match the text. Lines in (F) are Bragg rods, indicative of a random stacking along the 6-fold axis. Indexing residuals can be found in the Supporting Information.

dimensions relative to the copolymer dimensions (a = 31.1 nm; c/a = 1.633) are inconsistent with the C14 Laves phase discussed earlier, which bears the same $P6_3/mmc$ space group symmetry. Interestingly, the locations of the ($10\overline{1}0$) and ($11\overline{2}0$) HCP scattering reflections are coincident with the q^* and $\sqrt{3}$ q^* peaks observed on annealing for 66 h, indicating that the pattern observed in Figure 5A,C likely stemmed from a lack of long-range order perpendicular to the hexagonal planes. Indeed, as shown in Figure S4C, the faint scattering spots observed for $\phi_2 = 0.28$ after annealing at 120 °C agree well with a HCP phase assignment despite the distinct isotropy and higher relative intensities of the q^* and $\sqrt{3}$ q^* rings, a feature observed in multiple samples

annealed near the limiting S block T_g (Figure S4). For the studied SB3/SB5 blends with $\phi_2 = 0.31$, we note that the close proximity of the order-disorder transition temperature (150 °C < $T_{\rm ODT}$ < 180 °C) and the annealing temperature (T = 150 °C) coupled with the narrow window of close packing/DIS coexistence dictated by the Gibbs phase rule and a known variance between sample stage and hot plate temperature ($T \pm 5$ °C) likely impacted the ordering process. The FCC and HCP phases are nearly degenerate in free energy and subtle changes in processing could impact the resulting structure.⁸³ Therefore, the "HEXs" scattering pattern in Figure 5A,C does not necessarily reflect a precursor to the FCC or HCP phases.

As shown in Figure 6, close packing persisted to $\phi_2 = 0.41$, dominated by a HCP structure; indexed traces can be found in Figures 7A and S7. Lines in the 2D scattering data (Figure 7F), often referred to as Bragg rods, evidenced the presence of stacking faults along the 6-fold axis in some samples. 83 Increasing ϕ_2 to 0.46, led to a dense array of scattering reflections at both 150 and 180 °C (Figure 6). Indexing (Figures 7B and S8; Table S3) revealed σ/HCP phase coexistence, wherein $\langle R \rangle = 17.5$ nm for both phases (see Supporting Information for calculation details). Increasing ϕ_2 further to 0.51 and annealing at 180 °C for 66 h, generated scattering largely consistent with the $Pm\bar{3}n$ symmetry of the A15 phase, but additional densely clustered reflections complicate the phase assignment (Figure 6B). As shown in Figures 7D, these additional reflections can be reasonably explained by a coexisting σ phase bearing $P4_2/mnm$ symmetry and the same mean particle radius $\langle R \rangle = 17.6$ nm; more detailed indexing can be found in Figure S9 and Table S4. Annealing at 150 °C for the same 66 h yielded a scattering pattern with P126/mmc space group, which is associated with a QC (Figures 6A and 7C; Table S5). This state is largely found as a metastable precursor to the FK A15 and σ phases, evidencing increasing kinetic limitations with proximity to $T_{\rm g,PS} \approx 90$ °C and distance from the ODT (i.e., $T_{\rm ODT}-T$). 20,63,79 At $\phi_2=0.56$, SAXS

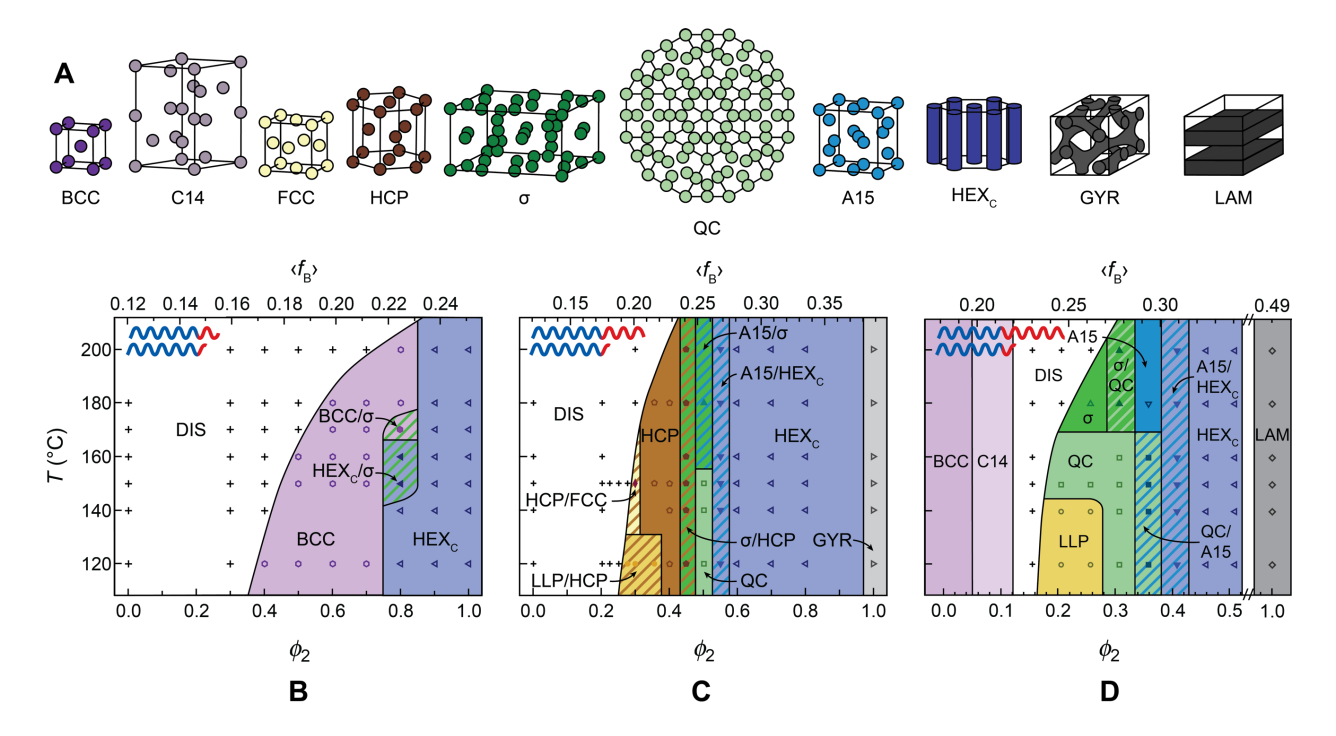


Figure 8. (A) Observed phases and (B-D) experimental phase portraits for bidisperse blends with increasing core block length difference. Phase portraits reflect SAXS data collected for (B) SB3/SB4 blends with $N_2/N_1 = 1.1$, (C) SB3/SB5 blends with $N_2/N_1 = 1.4$, and (D) SB1/SB2 blends with $N_2/N_1 = 1.6$. The results in (D) are superimposed over data from our previous report [63]. The schematics in the upper left corners of panels (B-D) display the difference in the constituent copolymer lengths. $\langle f_B \rangle$ and ϕ_2 are the volume fractions of 1,4-polybutadiene and the larger, more symmetric copolymer in the melt. DIS, LLP, BCC, FCC, HCP, QC, HEX_C, GYR, and LAM denote disorder, liquid-like packing, body-centered cubic, face-centered cubic, hexagonal close-packed, dodecagonal quasicrystal, hexagonally-packed cylinders, double gyroid, and lamellae, respectively. Phase coexistence in (B-D) is denoted by a striped background.

revealed a well-resolved P6/mm symmetry indicative of HEX_C, but in coexistence with another phase (Figure 6). Owing to the poor resolution of scattering reflections not associated with HEX_C, it is difficult to ascertain with certainty whether the pattern corresponds to σ , A15, or QC packing, particularly for T \leq 150 °C. However, the three intense reflections centered about q_{10,HEX_C} point to a HEX_C/A15 phase coexistence (Figure 7E; Table S6). As shown in Figure 6, a pure HEX_C phase window immediately follows, persisting for the remainder of the blends studied (0.61 $\leq \phi_2 \leq$ 0.81), and the pure SB5 ($\phi_2 = 1$) was found to adopt the $Ia\bar{3}d$ symmetry of the gyroid (GYR) phase.

Despite persistent phase coexistence and truncation of the FK phase window by close packing, SB3/SB5 blends afforded access to a wide range of nanostructures. Together with the BCC, C14, and LAM phases observed with blends of SB1 and SB2, the bidisperse blends studied in this work revealed at least 12 distinct morphologies: BCC, HCP, FCC, C14, σ , A15, QC, LLP, HEXc, GYR, LAM, and DIS. This is a remarkably complex array arising from binary blends prepared from a set of five polymers and highlights the utility of this approach in controlling phase behavior. Compiling the SAXS data into phase portraits (Figure 8), we can see that, with increasing difference in core block lengths the size and purity of the FK phase window increases. In addition, the OOT from particles to cylinders systematically shifts to higher core block fractions, increasing from $f_B = 0.20$ in the nominally single-component SB melt to $\langle f_B \rangle = 0.31$ for SB/SB' blends with $N_2/N_1 = 1.6$. Both results are expected as a difference in the block dispersities is well known to shift OOTs^{84,85} and FK phases are anticipated at high core fractions. However, less clear is why so much of the SCFT-predicted FK phase window was dominated by close-packing.

Phase Stabilization Mechanisms. Past studies have revealed two primary mechanisms by which addition of a second copolymer influences phase selection in blends with constant N_{corona} and variable N_{core} . First is the preference for a large, deformable core domain and an expanded particle phase window. This stems from the need to accommodate the larger copolymer, while simultaneously relaxing chain stretching constraints in the bidisperse core. This accommodation effect is especially evident in Figure 9, wherein we observe a linear increase in the mean particle radii with increasing ϕ_2 for all blends. However, more impactful is the latter, which, akin to conformational asymmetry, increases the deformability of the core domain and favors curvature at the core—corona interface, thus increasing the width of the particle packing window in terms of composition (see Figures 8 and 9B). The impact of these effects on the stability

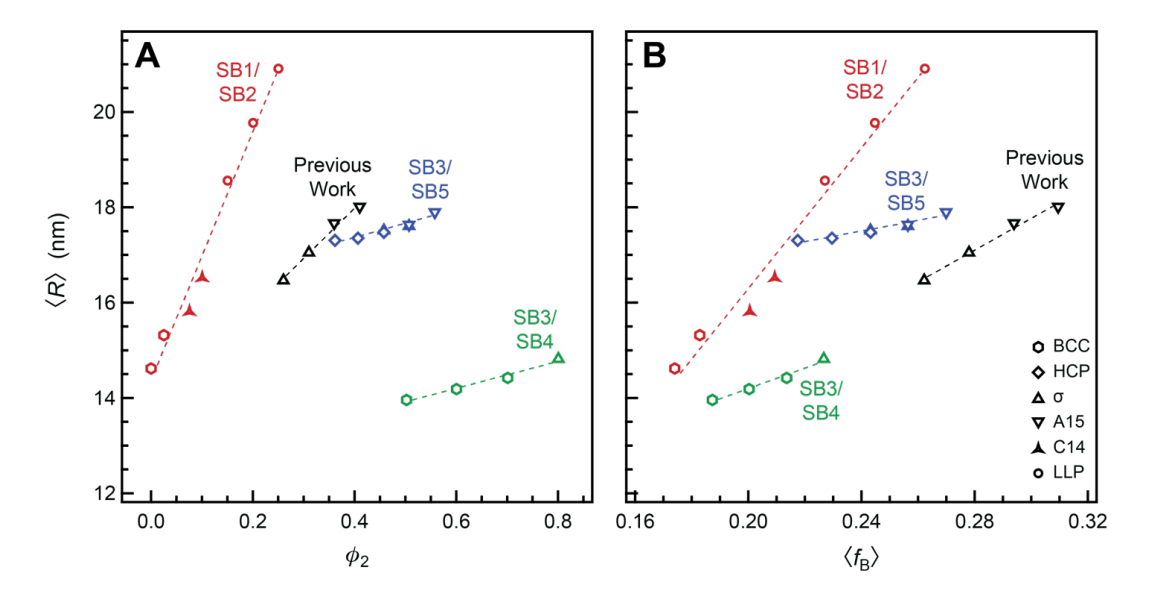


Figure 9. Mean particle radii $\langle R \rangle$ as a function of the volume fraction of (A) the larger copolymer ϕ_2 and (B) butadiene $\langle f_B \rangle$ for various blends and packings. Mean particle radii were calculated as discussed in the Supporting Information based on the unit cell volume derived from Bragg reflections at 180 °C, with the exception of the SB3/SB4 blends which reflect data collected at 150 °C. For a liquid-like packing (LLP), the particle radius was estimated taking the principal peak as the BCC (110) reflection. BCC, HCP, σ , A15, C14, and LLP are identified by hexagon, diamond, triangle, inverted triangle, cross, and circle markers. The dashed lines are linear fits of the particle radii in SB1/SB2 (red), SB3/SB4 (green), and SB3/SB5 (blue) blends in addition to the blends studied in our previous work (black) [63].

of A15 and σ packings has been widely explored for highly conformationally and/or architecturally asymmetric amphiphiles. 19,29,30,33,35,51–55,66 In essence, as the sphere–cylinder OOT is pushed to higher compositions, the σ phase emerges, offering a reduction in interfacial area, but eventually giving way to the A15 phase as the core fraction becomes more substantial. Whereas the σ phase minimizes interfacial area relative to the BCC phase, the preference for an A15 packing over the σ phase at high core fractions is not enthalpic in origin, as the A15 phase has a higher mean interfacial area at a constant mean particle radius; 49,50,53 a phase-dependent mean particle radius has been found in hydrated surfactants, 27,89,90 but was not observed here for any samples with A15/ σ phase coexistence (Figure 9). Rather, this preference appears to stem from increased constraints on the particle size distribution, which is much wider for the σ phase. Indeed, calculations performed by Reddy *et al.* revealed chain stretching penalties increase for the σ phase

relative to the A15 phase with increasing core fraction. This can be explained by a reduction in the configurational degrees of freedom of chains in the corona as the relative domain size decreases. This makes the domains more rigid and less accommodating of the broader particle size distribution of the σ phase.

The second mechanism influencing phase selection is the preferential segregation of each copolymer in the melt. Copolymer distribution is constrained by two limits: homogenous mixing and macrophase separation. These limits have been explored in some detail.86-88,91 For widely varying molecular weights (i.e., $N_2/N_1 \gg 1$) and compositions (i.e., $f_2 \gg f_1$), copolymer blends can macrophase separate into micron-scale domains rich in polymers 1 or 2. For a less dramatic dissimilarity in the copolymers, chains remain mixed and can be well-approximated as a singlecomponent system. 91 However, intermediate between these limits lie a number of possibilities for "partial" segregation of the two copolymers. One is a lateral segregation along an interface. For comparable blends to those studied herein, Liu et al. showed by SCFT that asymmetric and symmetric copolymers localize along the core–corona interface of the σ phase in regions of high and low curvature, respectively. 62 This stems from a preference to maintain the native interfacial area/chain for each diblock. A similar mechanism can also drive segregation of copolymers between micelles (i.e., micelles at different Wyckoff positions can have different ϕ_i). Curvature decreases with increasing micelle radius. As such, compositionally asymmetric copolymers will favor smaller micelles, whereas larger and/or more symmetric copolymers will favor larger micelles. This mechanism is supported experimentally. In bidisperse diblock copolymer blends with $f_1 \approx f_2$ and $N_2/N_1 \approx 7$, Koizumi and coworkers observed an unusual "superlattice" structure formed from a bidisperse, yet mixed population of micelles rich in polymers 1 or 2.88 In a third case, chains can segregate along the normal to the core-corona interface. For a vanishing interfacial width, differences in relative block lengths will require a radial distribution of diblock copolymer chains, with the shorter copolymer forming a "shell" around the core owing to its inability to fully extend to the center of the micelle. Last is a partial dissolution of one copolymer into a single nanodomain, analogous to a small homopolymer. This might be expected for a very weakly segregated copolymer (*i.e.*, low N and f). Together, these mechanisms greatly increase the degrees of freedom for the blended system, alleviating the chain stretching penalties imposed on adopting a broader particle size distribution and making the σ , A15, C14, and C15 phases more favorable.

Still unexplained is why a large window of close packing was observed for SB3/SB5 blends preceding the σ phase window. To explore this issue, we performed SCFT calculations, including FCC and HCP phases as candidate structures. As seen in Figure 10, results were largely in agreement with experiments; temperature in Figure 9A was rescaled as $\chi(N)$, where $\chi_{SB} = 52.8/T$ -0.070 based on $T_{\rm ODT}$ data collected for a series of symmetric SB diblock copolymers and a segment volume $v = 118 \text{ Å}^{3.56,92}$ With increasing ϕ_2 , SCFT predicts a large close-packed phase window followed by a narrow region of σ/HCP phase coexistence, a pure σ phase, and σ/HEX_C , A15/HEX_C, or HCP/HEX_C phase coexistence, after which pure HEX_C and GYR phases emerge. Two-phase windows dictated by the Gibbs phase rule between adjacent A15, σ , and HCP windows were vanishingly small in contrast to experiment, where the A15 and σ phases were only observed in coexistence with other phases. This is somewhat surprising given that the experimental FK phase window extends to lower ϕ_2 , but it could arise due to kinetic limitations or a discrepancy in $\chi(N)$. SCFT revealed the particle phases to be nearly degenerate in free energy (Figure S10). Moreover, canonical SCFT calculations performed for $30 \le \chi(N) \le 40$ (Figure S12) exposed a widening FK phase window with increasing $\chi(N)$, as the close-packed window is pushed to lower

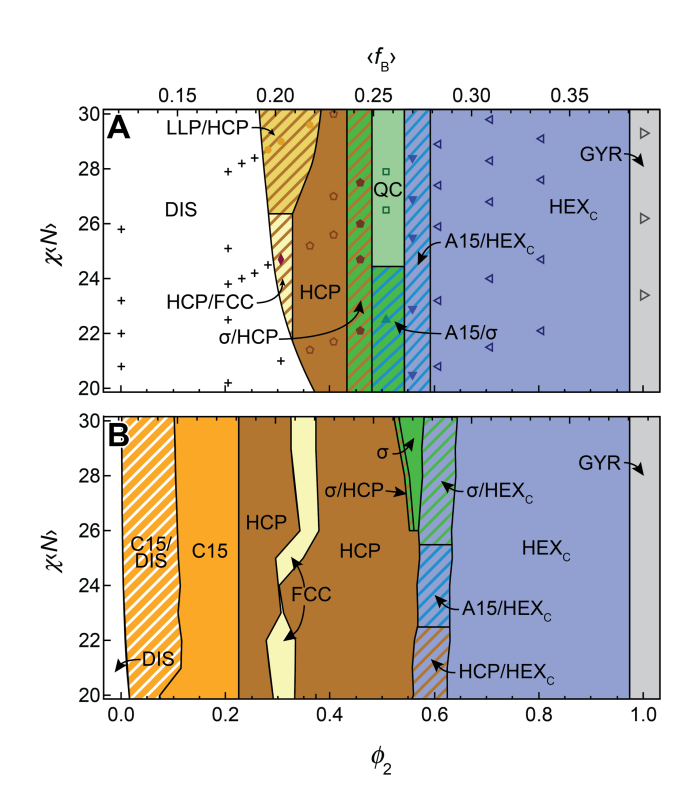


Figure 10. (A) Experiment and (B) SCFT derived phase portraits for bidisperse blends of the type AB/AB' with $N_2/N_1 = 1.4$, $f_{B,1} = 0.12$, $f_{B,2} = 0.39$, and $\varepsilon = 1.7$. The experimental phase portrait in Figure 6C derived from SB3/SB5 blends is reproduced in (A) with temperature rescaled as $\chi(N)$ (see text for details). $\langle f_B \rangle$ and ϕ_2 are the volume fractions of the minority domain and the larger, more symmetric copolymer in the melt. DIS, LLP, FCC, HCP, QC, HEX_C, and GYR denote disorder, liquid-like packing, face-centered cubic, hexagonal close-packed, dodecagonal quasicrystal, hexagonally-packed cylinders, and double gyroid, respectively. Phase coexistence is denoted by a striped background.

 ϕ_2 . The principal discrepancy is in the phase behavior at low ϕ_2 . Experimentally our system was disordered for $\phi_2 < 0.28$, but SCFT predicts a transition to Laves phases, suggesting that the close-packed phase window occurs intermediate to the Laves and σ phase windows. A discrepancy in the ODT between experiment and mean-field theory is expected as fluctuation effects at finite N are well-known to truncate the mean-field phase portrait. However, the SCFT prediction and experimental observation of a close-packed window intermediate between the Laves and σ phase windows conflicts with arguments invoked to rationalize the emergence of FK phases, namely that their emergence is driven enthalpically^{49,50} (*i.e.*, a minimization of interfacial area) and/or by a favorable distribution in micelle volume.^{59-61,65} The FCC and HCP phases are both (1)

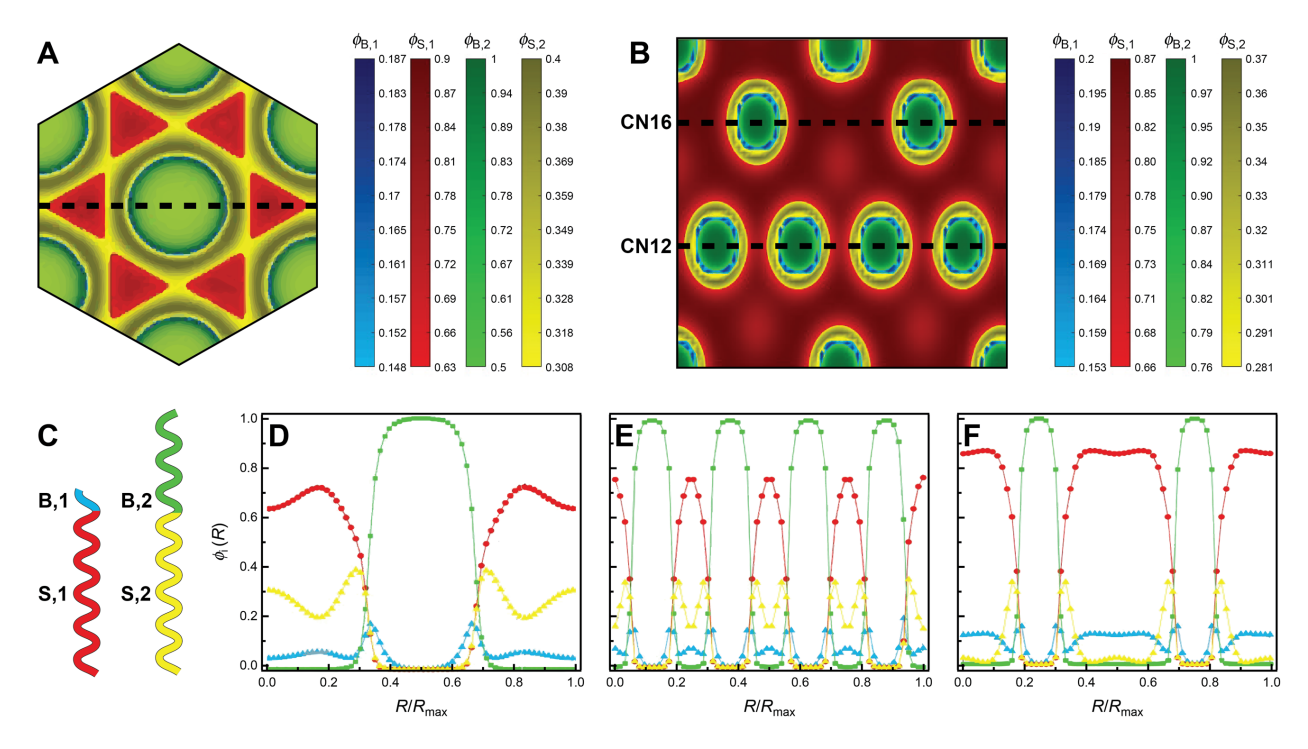


Figure 11. Composition maps for the (A) (0001) HCP and (B) (110) C15 planes and 1D composition profiles in the (D) HCP [$\bar{1}100$] and (E,F) C15 [$1\bar{1}1$] directions. Data were calculated *via* SCFT for SB3/SB5 blends with (A,D) $\phi_2 = 0.40$ and (B,E,F) 0.20 at $\chi(N) = 30$. ϕ_i is the volume fraction of block i at each position. R/R_{max} is the nondimensional distance along the dashed lines in (A,B), where 0 and 1 correspond to the left and right edge of the composition map. The 1D composition profiles along the lines of CN12 and CN16 are shown in (E) and (F), respectively. The schematic in (C) shows the relative copolymer block lengths. Blue and red shading correspond to the B and S blocks of SB3, whereas green and yellow shading correspond to the B and S blocks of SB5, respectively.

characterized by a unimodal particle size distribution and (2), assuming minimal coronal overlap, less spherical particles.⁹³ Nonetheless, this balance changes if the block junction is no longer constrained to the interface.

As shown in Figures 11A and D, SCFT predicts a significant fraction of the smaller copolymer leaves the interface and swells the corona, due to its low degree of segregation and compositional asymmetry. This reduces the range of the repulsive intermicellar potential responsible for imposition of the Wigner-Seitz geometry onto the particle. In effect, the enthalpic gain obtained aon adopting a BCC phase or any of the FK phases is minimized. This is particularly evident in Figures 11A and D, where it can be seen that the smaller copolymer fills the octahedral voids in

the HCP lattice, eliminating the need for chains tethered to the core—corona interface to stretch to the vertices of the Wigner-Seitz polyhedron and allowing the core to remain spherical. It is well-known that addition of solvent or homopolymer to the corona domain favors close-packing by similar phenomena: alleviating packing constraints and reducing the range of the repulsive intermicellar potential. 83,94–96 Indeed, even the preference for a HCP lattice shown here mirrors the homopolymer case. The octahedral interstitial sites of the HCP lattice are larger than the tetrahedral sites of the FCC phase and, therefore, can more easily accommodate larger additives within the corona. 97

We now turn to the occurrence of Laves phases at low fractions of the larger copolymer focusing on two cases: (1) both polymers are constrained to the core–corona interface and (2) one polymer is partially dissolved in the matrix. For a well-segregated system, such as the SB1/SB2 blends studied in this work, at low ϕ_2 there is a conflict between the size of the larger copolymer and the size of the core domain, which is constrained by the low overall core fraction and the smaller preferred core radius of the more prevalent asymmetric copolymer. This competition stabilizes a bidisperse particle size distribution to minimize unfavorable stretching and compression of the asymmetric and symmetric copolymers, respectively. A key factor is that a bidisperse particle size distribution is incompatible with the BCC phase and therefore the C14 and C15 Laves phases emerge, as observed in blends of SB1 and SB2. However, this competition is delicate: an inhomogenous copolymer distribution comes at an entropic cost and Laves phases require an A₂B stoichiometry of small (A) and large (B) particles.⁴⁸ As the fraction of the larger copolymer increases, an increasing core fraction and radius more easily accommodate the larger chains, increasing the favorability of a narrower particle size distribution. Moreover, owing to the relatively high composition of the core block, the fraction of the core pervaded by the larger copolymer ($\phi_{2,core}$) increases more quickly than ϕ_2 ($\phi_{2,core} \approx \phi_2 f_{B,2} / \langle f_B \rangle$, where $f_{B,2} / \langle f_B \rangle \ge 1$). This requires an increase in the fraction of large micelles, resulting in a divergence from the A₂B stoichiometry of the Laves phases. Together these effects decrease the stability of the Laves phases with increasing ϕ_2 , favoring the σ phase.⁶⁵ However, this mechanism fails to explain the SCFT prediction of Laves phases at low ϕ_2 for SB3/SB5 blends, as the asymmetric copolymer is completely disordered and therefore too poorly segregated to form micelles on its own.

As shown in Figure 11B, SCFT predicts a negligible difference in the core radius for particles in the CN12 and CN16 sites of the C15 phase, despite a large difference in the site volumes. Along a line of CN12 lattice sites, the calculated 1D composition profile (Figure 11E) reveals a particle radius dictated largely by the dimensions of the symmetric copolymer, with only a modest fraction of the asymmetric core block delocalized from the interface and swelling the core domain. In contrast, for the larger CN16 sites, the interparticle corona domains constituted by the symmetric copolymer are separated by a large domain, rich in the asymmetric copolymer (Figure 11F). In effect, the variance in the site volume is mediated by delocalization of the smaller copolymer away from the core-corona interface and into the void space of the larger CN16 lattice sites. This prediction is curious given the absence of Laves phases in Takagi and Yamamoto's work on ABdiblock copolymer/B-homopolymer blends, wherein A and B denote the core and corona chemistries, respectively.⁵⁸ However, in the dry-brush regime (i.e., where α = $N_{\rm B,homopolymer}/N_{\rm B,diblock} > 1$ and homopolymer does not swell the corona block), the native preferred interfacial area per chain of the only modestly off-symmetric copolymer prevented access to particles. For the currently studied bidisperse blends, the asymmetric copolymer drives additional interfacial curvature; a similar effect may also be observed in high AB-diblock copolymer/Bhomopolymer blends wherein the diblock copolymer is more asymmetric and forms particles.

Lastly, delocalization of copolymer from the interface also favors close packing. Why does SCFT predict the C15 Laves phase to be stable over the HCP or FCC phases? We suspect that this is due to the need for a more significant void volume at high fractions of the asymmetric copolymer. Interstitial voids are larger in the C15 phase than the HCP or FCC phases and, therefore, offer an increase in the configurational entropy for asymmetric chains untethered from the interface. As the fraction of the symmetric copolymer is increased, the volume of asymmetric copolymer that needs to be accommodated is decreased and close-packing emerges. Reducing the fraction of the asymmetric copolymer further decreases the fraction of copolymer in the matrix, expanding the range of the repulsive intermicellar potential and favoring the σ and A15 phases (see Figure S13 for σ and A15 phase composition maps).

CONCLUSIONS

We have shown that blending two diblock copolymers with constant corona block lengths and variable core block lengths allows access to almost every nanostructure observed to date in diblock copolymer melts: BCC, HCP, FCC, C14, σ , A15, QC, LLP, HEX_C, GYR, LAM, and DIS. This strategy is simple, and unlike previous routes to FK phases in particular, should be amenable to a wide range of block chemistries. Just a modest distribution of block lengths in the core is sufficient to drive formation of the σ phase and the phase behavior can be readily tuned in bidisperse diblock copolymer blends by varying the relative core block lengths or the segregation of the more asymmetric copolymer (*i.e.*, *via N* and *f*). This work adds to the growing list of strategies by which many of these complex packings can be accessed, ^{19,20,30–32,45,52–66} improving our control of structure at the nanoscale.

ASSOCIATED CONTENT

The Supporting Information is available free of charge at: [inset url]

Experimental details and additional characterization data (PDF)

AUTHOR INFORMATION

Corresponding Author

Frank S. Bates – Department of Chemical Engineering and Materials Science, University of Minnesota, Minnesota, Minnesota 55455, United States; orcid.org/0000-0003-3977-1278; Email: bates001@umn.edu

Authors

Aaron P. Lindsay – Department of Chemical Engineering and Materials Science, University of Minnesota, Minnesota, Minnesota 55455, United States; orcid.org/0000-0003-0223-193X

Guo Kang Cheong – Department of Chemical Engineering and Materials Science, University of Minnesota, Minnesota 55455, United States; orcid.org/0000-0003-0814-9849

Austin J. Peterson – Department of Chemical Engineering and Materials Science, University of Minnesota, Minnesota, Minnesota 55455, United States; orcid.org/0000-0001-8818-1333

Steven Weigand – DND-CAT Synchrotron Research Center, Northwestern University, APS/ANL Building 432-A004, 9700 South Cass Ave, Argonne, Illinois 60439, United States; orcid.org/0000-0003-3137-0672

Kevin D. Dorfman – Department of Chemical Engineering and Materials Science, University of Minnesota, Minnesota, Minnesota 55455, United States; orcid.org/0000-0003-0065-5157

Timothy P. Lodge – Department of Chemical Engineering and Materials Science and Department of Chemistry, University of Minnesota, Minneapolis, Minnesota 55455, United States; orcid.org/0000-0001-5916-8834

Notes

The authors declare no competing financial interest.

ACKNOWLEDGMENTS

This work was supported by the National Science Foundation under Grants No. DMR-1801993 (A.P.L., A.J.P., F.S.B.) and DMR-1719692 (G.K.C., F.S.B., K.D.D.) as well as a National Science Foundation Graduate Research Fellowship under Grant No. 00039202 (A.P.L.). We extend our gratitude to the staff at Sector 5 for their assistance in conducting these experiments during the pandemic. SAXS experiments were performed at Sectors 5 and 12 of the Advanced Photon Source (APS). The DuPont-Northwestern-Dow Collaborative Access Team (DND-CAT) located at Sector 5 is supported by Northwestern University, the Dow Chemical Company, and DuPont de Nemours, Inc. The APS is a U.S. Department of Energy (DOE) Office of Science User Facility operated for the DOE Office of Science by Argonne National Laboratory under Contract No. DE-AC02-06CH11357. Data was collected using an instrument at Sector 5 funded by the National Science Foundation under Award Number 0960140. Parts of this work were carried out in the Characterization Facility at the University of Minnesota, which receives partial support from the NSF through the MRSEC program, DMR-2011401.

REFERENCES

- (1) Leibler, L. Theory of Microphase Separation in Block Copolymers. *Macromolecules* **1980**, *13*, 1602–1617. https://doi.org/10.1021/ma60078a047.
- (2) Hajduk, D. A.; Harper, P. E.; Gruner, S. M.; Honeker, C. C.; Kim, G.; Thomas, E. L.; Fetters, L. J. The Gyroid: A New Equilibrium Morphology in Weakly Segregated Diblock Copolymers. *Macromolecules* **1994**, *27*, 4063–4075. https://doi.org/10.1021/ma00093a006.
- (3) Tyler, C. A.; Morse, D. C. Orthorhombic *Fddd* Network in Triblock and Diblock Copolymer Melts. *Phys. Rev. Lett.* **2005**, *94*, 208302. https://doi.org/10.1103/PhysRevLett.94.208302.
- (4) Takenaka, M.; Wakada, T.; Akasaka, S.; Nishitsuji, S.; Saijo, K.; Shimizu, H.; Kim, M. I.; Hasegawa, H. Orthorhombic *Fddd* Network in Diblock Copolymer Melts. *Macromolecules* **2007**, *40*, 4399–4402. https://doi.org/10.1021/ma070739u.
- (5) Edwards, S. F. The Statistical Mechanics of Polymers with Excluded Volume. *Proc. Phys. Soc.* **1965**, *85*, 613–624.
- (6) Helfand, E.; Tagami, Y. Theory of the Interface between Immiscible Polymers. II. *J. Chem. Phys.* **1972**, *56*, 3592–3601. https://doi.org/10.1002/polb.1996.930.
- (7) Helfand, E.; Wasserman, Z. R. Block Copolymer Theory. 4. Narrow Interphase Approximation. *Macromolecules* **1976**, *9*, 879–888.
- (8) Fredrickson, G. H.; Helfand, E. Fluctuation Effects in the Theory of Microphase Separation in Block Copolymers. *J. Chem. Phys.* **1987**, *87*, 697–705. https://doi.org/10.1063/1.453566.
- (9) Matsen, M. W.; Bates, F. S. Unifying Weak- and Strong-Segregation Block Copolymer Theories. *Macromolecules* **1996**, *29*, 1091–1098. https://doi.org/10.1021/ma951138i.
- (10) Skoulios, A. E.; Tsouladze, G.; Franta, E. Configuration Des Chaînes Macromoléculaires Des Copolymères Sequences En Solution Concentree. Exemple Des Copolymeres Séquencés Polystyroléne–Polyoxyéthyléne et Polyoxypropylène–Polyoxyéthylène En Solution Dans Des Solvants Préférentiels de l'une Ou l'aut. *J. Polym. Sci. Part C Polym. Symp.* **1963**, *4*, 507–518.
- (11) Inoue, T.; Soen, T.; Hashimoto, T. Thermodynamic Interpretation of Domain Structure in Solvent-Cast Films of a-B Type Block Copolymers of Styrene and Isoprene. *J. Polym. Sci. Part A-2 Polym. Phys.* **1969**, *7*, 1283–1302. https://doi.org/10.1002/pol.1969.160070801.
- (12) Khandpur, A. K.; Förster, S.; Bates, F. S.; Hamley, I. W.; Ryan, A. J.; Bras, W.; Almdal, K.; Mortensen, K. Polyisoprene–Polystyrene Diblock Copolymer Phase Diagram near the Order–Disorder Transition. *Macromolecules* 1995, 28, 8796–8806. https://doi.org/10.1021/ma00130a012.
- (13) Bates, F. S.; Cohen, R. E.; Berney, C. V. Small-Angle Neutron Scattering Determination of Macrolattice Structure in a Polystyrene-Polybutadiene Diblock Copolymer. *Macromolecules* **1982**, *15*, 589–592. https://doi.org/10.1021/ma00230a073.

- (14) Huang, Y.-Y.; Hsu, J.-Y.; Chen, H.-L.; Hashimoto, T. Existence of FCC-Packed Spherical Micelles in Diblock Copolymer Melt. *Macromolecules* **2007**, *40*, 406–409. https://doi.org/10.1021/ma062149m.
- (15) Hsu, N. W.; Nouri, B.; Chen, L. T.; Chen, H. L. Hexagonal Close-Packed Sphere Phase of Conformationally Symmetric Block Copolymer. *Macromolecules* **2020**, *53*, 9665–9675. https://doi.org/10.1021/acs.macromol.0c01445.
- (16) Uddin, M. H.; Rodriguez, C.; López-Quintela, A.; Leisner, D.; Solans, C.; Esquena, J.; Kunieda, H. Phase Behavior and Microstructure of Poly(Oxyethylene)–Poly(Dimethylsiloxane) Copolymer Melt. *Macromolecules* **2003**, *36*, 1261–1271. https://doi.org/10.1021/ma0210978.
- (17) Lee, S.; Bluemle, M. J.; Bates, F. S. Discovery of a Frank-Kasper σ Phase in Sphere-Forming Block Copolymer Melts. *Science* **2010**, *330*, 349–353. https://doi.org/10.1126/science.1195552.
- (18) Kim, K.; Schulze, M. W.; Arora, A.; Lewis, R. M.; Hillmyer, M. A.; Dorfman, K. D.; Bates, F. S. Thermal Processing of Diblock Copolymer Melts Mimics Metallurgy. *Science* **2017**, *356*, 520–523. https://doi.org/10.1126/science.aam7212.
- (19) Bates, M. W.; Lequieu, J.; Barbon, S. M.; Lewis, R. M.; Delaney, K. T.; Anastasaki, A.; Hawker, C. J.; Fredrickson, G. H.; Bates, C. M. Stability of the A15 Phase in Diblock Copolymer Melts. *Proc. Natl. Acad. Sci. U. S. A.* **2019**, *116*, 13194–13199. https://doi.org/10.1073/pnas.1900121116.
- (20) Gillard, T. M.; Lee, S.; Bates, F. S. Dodecagonal Quasicrystalline Order in a Diblock Copolymer Melt. *Proc. Natl. Acad. Sci. U. S. A.* **2016**, *113*, 5167–5172. https://doi.org/10.1073/pnas.1601692113.
- (21) Zhang, J.; Sides, S.; Bates, F. S. Ordering of Sphere Forming SISO Tetrablock Terpolymers on a Simple Hexagonal Lattice. *Macromolecules* **2012**, *45*, 256–265. https://doi.org/10.1021/ma202196c.
- (22) Chanpuriya, S.; Kim, K.; Zhang, J.; Lee, S.; Arora, A.; Dorfman, K. D.; Delaney, K. T.; Fredrickson, G. H.; Bates, F. S. Cornucopia of Nanoscale Ordered Phases in Sphere-Forming Tetrablock Terpolymers. *ACS Nano* **2016**, *10*, 4961–4972. https://doi.org/10.1021/acsnano.6b00495.
- (23) Miyamori, Y.; Suzuki, J.; Takano, A.; Matsushita, Y. Periodic and Aperiodic Tiling Patterns from a Tetrablock Terpolymer System of the A 1 BA 2 C Type. *ACS Macro Lett.* **2020**, *9*, 32–37. https://doi.org/10.1021/acsmacrolett.9b00861.
- (24) Hayashida, K.; Dotera, T.; Takano, A.; Matsushita, Y. Polymeric Quasicrystal: Mesoscopic Quasicrystalline Tiling in ABC Star Polymers. *Phys. Rev. Lett.* **2007**, *98*, 195502. https://doi.org/10.1103/PhysRevLett.98.195502.

- (25) Hayashida, K.; Takano, A.; Dotera, T.; Matsushita, Y. Giant Zincblende Structures Formed by an ABC Star-Shaped Terpolymer/Homopolymer Blend System. *Macromolecules* **2008**, *41*, 6269–6271. https://doi.org/10.1021/ma801367v.
- (26) Vargas, R.; Mariani, P.; Gulik, A.; Luzzati, V. Cubic Phases of Lipid-Containing Systems. The Structure of Phase Q223 (Space Group Pm3n). An X-Ray Scattering Study. *J. Mol. Biol.* **1992**, *225*, 137–145. https://doi.org/10.1016/0022-2836(92)91031-J.
- (27) Kim, S. A.; Jeong, K. J.; Yethiraj, A.; Mahanthappa, M. K. Low-Symmetry Sphere Packings of Simple Surfactant Micelles Induced by Ionic Sphericity. *Proc. Natl. Acad. Sci. U. S. A.* **2017**, *114*, 4072–4077. https://doi.org/10.1073/pnas.1701608114.
- (28) Baez-Cotto, C. M.; Mahanthappa, M. K. Micellar Mimicry of Intermetallic C14 and C15 Laves Phases by Aqueous Lyotropic Self-Assembly. *ACS Nano* **2018**, *12*, 3226–3234. https://doi.org/10.1021/acsnano.7b07475.
- (29) Balagurusamy, V. S. K.; Ungar, G.; Percec, V.; Johansson, G. Rational Design of the First Spherical Supramolecular Dendrimers Self-Organized in a Novel Thermotropic Cubic Liquid-Crystalline Phase and the Determination of Their Shape by X-Ray Analysis. *J. Am. Chem. Soc.* **1997**, *119*, 1539–1555. https://doi.org/10.1021/ja963295i.
- (30) Ungar, G.; Liu, Y.; Zeng, X.; Percec, V.; Cho, W.-D. Giant Supramolecular Liquid Crystal Lattice. *Science* **2003**, *299*, 1208–1211. https://doi.org/10.1007/springerreference_11442.
- (31) Zeng, X.; Ungar, G.; Liu, Y.; Percec, V.; Dulcey, A. E.; Hobbs, J. K. Supramolecular Dendritic Liquid Quasicrystals. *Nature* **2004**, *428*, 157–160. https://doi.org/10.1038/nature02368.
- (32) Huang, M.; Hsu, C. H.; Wang, J.; Mei, S.; Dong, X.; Li, Y.; Li, M.; Liu, H.; Zhang, W.; Aida, T.; et al. Selective Assemblies of Giant Tetrahedra via Precisely Controlled Positional Interactions. *Science* **2015**, *348*, 424–428. https://doi.org/10.1126/science.aaa2421.
- (33) Yue, K.; Huang, M.; Marson, R. L.; Hec, J.; Huang, J.; Zhou, Z.; Wang, J.; Liu, C.; Yan, X.; Wu, K.; et al. Geometry Induced Sequence of Nanoscale Frank-Kasper and Quasicrystal Mesophases in Giant Surfactants. *Proc. Natl. Acad. Sci. U. S. A.* **2016**, *113*, 14195–14200. https://doi.org/10.1073/pnas.1609422113.
- (34) Su, Z.; Hsu, C. H.; Gong, Z.; Feng, X.; Huang, J.; Zhang, R.; Wang, Y.; Mao, J.; Wesdemiotis, C.; Li, T.; et al. Identification of a Frank–Kasper Z Phase from Shape Amphiphile Self-Assembly. *Nat. Chem.* **2019**, *11*, 899–905. https://doi.org/10.1038/s41557-019-0330-x.
- (35) Su, Z.; Huang, J.; Shan, W.; Yan, X.-Y.; Zhang, R.; Liu, T.; Liu, Y.; Guo, Q.-Y.; Bian, F.; Miao, X.; et al. Constituent Isomerism-Induced Quasicrystal and Frank–Kasper σ Superlattices Based on Nanosized Shape Amphiphiles. *CCS Chem.* **2020**, *2*, 1434–1444. https://doi.org/10.31635/ccschem.020.202000338.

- (36) Liu, Y.; Liu, T.; Yan, X.; Guo, Q.-Y.; Wang, J.; Zhang, R.; Zhang, S.; Su, Z.; Huang, J.; Liu, G.-X.; et al. Mesoatom Alloys via Self-Sorting Approach of Giant Molecules Blends. *Giant* **2020**, *4*, 100031. https://doi.org/10.1016/j.giant.2020.100031.
- (37) Bergman, G.; Shoemaker, D. P. The Determination of the Crystal Structure of the σ Phase in the Iron–Chromium and Iron–Molybdenum Systems. *Acta Crystallogr.* **1954**, *7*, 857–865. https://doi.org/10.1107/s0365110x54002605.
- (38) Yang, L.; Tulk, C. A.; Klug, D. D.; Moudrakovski, I. L.; Ratcliffe, C. I.; Ripmeester, J. A.; Chakoumakos, B. C.; Ehmd, L.; Martin, C. D.; Parise, J. B. Synthesis and Characterization of a New Structure of Gas Hydrate. *Proc. Natl. Acad. Sci. U. S. A.* **2009**, *106*, 6060–6064. https://doi.org/10.1073/pnas.0809342106.
- (39) Takeya, S.; Kamata, Y.; Uchida, T.; Nagao, J.; Ebinuma, T.; Narita, H.; Hori, A.; Hondoh, T. Coexistence of Structure I and II Hydrates Formed from a Mixture of Methane and Ethane Gases. *Can. J. Phys.* **2003**, *81*, 479–484. https://doi.org/10.1139/p03-038.
- (40) Weaire, D.; Phelan, R. A Counter-Example to Kelvin's Conjecture on Minimal Surfaces. *Philos. Mag. Lett.* **1994**, *69*, 107–110. https://doi.org/10.1080/09500839408241577.
- (41) Rivier, N. Kelvin's Conjecture on Minimal Froths and the Counter-Example of Weaire and Phelan. *Philos. Mag. Lett.* **1994**, *69*, 297–303. https://doi.org/10.1080/09500839408241607.
- (42) Gabbrielli, R.; Meagher, A. J.; Weaire, D.; Brakke, K. A.; Hutzler, S. An Experimental Realization of the Weaire-Phelan Structure in Monodisperse Liquid Foam. *Philos. Mag. Lett.* **2012**, *92*, 1–6. https://doi.org/10.1080/09500839.2011.645898.
- (43) Montis, R.; Fusaro, L.; Falqui, A.; Hursthouse, M. B.; Tumanov, N.; Coles, S. J.; Threlfall, T. L.; Horton, P. N.; Sougrat, R.; Lafontaine, A.; et al. Complex Structures Arising from the Self-Assembly of a Simple Organic Salt. *Nature* **2021**, *590*, 275–278. https://doi.org/10.1038/s41586-021-03194-y.
- (44) Xie, S.; Lindsay, A. P.; Bates, F. S.; Lodge, T. P. Formation of a C15 Laves Phase with a Giant Unit Cell in Salt-Doped A/B/AB Ternary Polymer Blends. *ACS Nano* **2020**, *14*, 13754–13764. https://doi.org/10.1021/acsnano.0c06071.
- (45) Klatt, M. A.; Steinhardt, P. J.; Torquato, S. Phoamtonic Designs Yield Sizeable 3D Photonic Band Gaps. *Proc. Natl. Acad. Sci. U. S. A.* **2019**, *116*, 23480–23486. https://doi.org/10.1073/pnas.1912730116.
- (46) Frank, F. C.; Kasper, J. S. Complex Alloy Structures Regarded as Sphere Packings. I. Definitions and Basic Principles. *Acta Crystallogr.* **1958**, *11*, 184–190. https://doi.org/10.1107/s0365110x58000487.
- (47) Frank, F. C.; Kasper, J. S. Complex Alloy Structures Regarded as Sphere Packings. II. Analysis and Classification of Representative Structures. *Acta Crystallogr.* **1959**, *12*, 483–499. https://doi.org/10.1107/s0365110x59001499.
- (48) De Graef, M.; McHenry, M. E. *Structure of Materials: An Introduction to Crystallography, Diffraction and Symmetry*, 2nd Ed.; Cambridge University Press: New York, 2012.

- (49) Lee, S.; Leighton, C.; Bates, F. S. Sphericity and Symmetry Breaking in the Formation of Frank-Kasper Phases from One Component Materials. *Proc. Natl. Acad. Sci. U. S. A.* **2014**, *111*, 17723–17731. https://doi.org/10.1073/pnas.1408678111.
- (50) Reddy, A.; Buckley, M. B.; Arora, A.; Bates, F. S.; Dorfman, K. D.; Grason, G. M. Stable Frank-Kasper Phases of Self-Assembled, Soft Matter Spheres. *Proc. Natl. Acad. Sci. U. S. A.* **2018**, *115*, 10233–10238. https://doi.org/10.1073/pnas.1809655115.
- (51) Chang, A. B.; Bates, F. S. Impact of Architectural Asymmetry on Frank-Kasper Phase Formation in Block Polymer Melts. *ACS Nano* **2020**, *14*, 11463–11472. https://doi.org/10.1021/acsnano.0c03846.
- (52) Bates, M. W.; Barbon, S. M.; Levi, A. E.; Lewis, R. M.; Beech, H. K.; Vonk, K. M.; Zhang, C.; Fredrickson, G. H.; Hawker, C. J.; Bates, C. M. Synthesis and Self-Assembly of AB_n Miktoarm Star Polymers. *ACS Macro Lett.* **2020**, *9*, 396–403. https://doi.org/10.1021/acsmacrolett.0c00061.
- (53) Xie, N.; Li, W.; Qiu, F.; Shi, A. C. σ Phase Formed in Conformationally Asymmetric AB-Type Block Copolymers. *ACS Macro Lett.* **2014**, *3*, 909–910. https://doi.org/10.1021/mz500445v.
- (54) Schulze, M. W.; Lewis, R. M.; Lettow, J. H.; Hickey, R. J.; Gillard, T. M.; Hillmyer, M. A.; Bates, F. S. Conformational Asymmetry and Quasicrystal Approximants in Linear Diblock Copolymers. *Phys. Rev. Lett.* **2017**, *118*, 207801. https://doi.org/10.1103/PhysRevLett.118.207801.
- (55) Mueller, A. J.; Lindsay, A. P.; Jayaraman, A.; Lodge, T. P.; Mahanthappa, M. K.; Bates, F. S. Quasicrystals and Their Approximants in a Crystalline-Amorphous Diblock Copolymer. *Macromolecules* 2021, 54, 2647–2660. https://doi.org/10.1021/acs.macromol.0c02871.
- (56) Lewis, R. M.; Arora, A.; Beech, H. K.; Lee, B.; Lindsay, A. P.; Lodge, T. P.; Dorfman, K. D.; Bates, F. S. Role of Chain Length in the Formation of Frank-Kasper Phases in Diblock Copolymers. *Phys. Rev. Lett.* **2018**, *121*, 208002. https://doi.org/10.1103/PhysRevLett.121.208002.
- (57) Takagi, H.; Hashimoto, R.; Igarashi, N.; Kishimoto, S.; Yamamoto, K. Frank-Kasper σ Phase in Polybutadiene-Poly(ε-Caprolactone) Diblock Copolymer/Polybutadiene Blends. *J. Phys. Condens. Matter* **2017**, *29*, 204002. https://doi.org/10.1088/1361-648X/aa6908.
- (58) Takagi, H.; Yamamoto, K. Phase Boundary of Frank-Kasper σ Phase in Phase Diagrams of Binary Mixtures of Block Copolymers and Homopolymers. *Macromolecules* **2019**, *52*, 2007–2014. https://doi.org/10.1021/acs.macromol.8b02356.
- (59) Mueller, A. J.; Lindsay, A. P.; Jayaraman, A.; Lodge, T. P.; Mahanthappa, M. K.; Bates, F. S. Emergence of a C15 Laves Phase in Diblock Polymer/Homopolymer Blends. *ACS Macro Lett.* 2020, *9*, 576–582. https://doi.org/10.1021/acsmacrolett.0c00124.

- (60) Cheong, G. K.; Bates, F. S.; Dorfman, K. D. Symmetry Breaking in Particle-Forming Diblock Polymer/Homopolymer Blends. *Proc. Natl. Acad. Sci. U. S. A.* **2020**, *117*, 16764–16769. https://doi.org/10.1073/pnas.2006079117.
- (61) Xie, J.; Shi, A.-C. Formation of Complex Spherical Packing Phases in Diblock Copolymer/Homopolymer Blends. *Giant* **2021**, *5*, 100043. https://doi.org/10.1016/j.giant.2020.100043.
- (62) Liu, M.; Qiang, Y.; Li, W.; Qiu, F.; Shi, A. C. Stabilizing the Frank-Kasper Phases via Binary Blends of AB Diblock Copolymers. *ACS Macro Lett.* **2016**, *5*, 1167–1171. https://doi.org/10.1021/acsmacrolett.6b00685.
- (63) Lindsay, A. P.; Lewis, R. M.; Lee, B.; Peterson, A. J.; Lodge, T. P.; Bates, F. S. A15, σ, and a Quasicrystal: Access to Complex Particle Packings via Bidisperse Diblock Copolymer Blends. *ACS Macro Lett.* **2020**, *9*, 197–203. https://doi.org/10.1021/acsmacrolett.9b01026.
- (64) Yamamoto, K.; Takagi, H. Frank-Kasper σ and A-15 Phases Formed in Symmetry and Asymmetry Block Copolymer Blend System. *Mater. Trans.* **2020**, *62*, 325–328. https://doi.org/10.2320/matertrans.mt-mb2020002.
- (65) Kim, K.; Arora, A.; Lewis, R. M.; Liu, M.; Li, W.; Shi, A. C.; Dorfman, K. D.; Bates, F. S. Origins of Low-Symmetry Phases in Asymmetric Diblock Copolymer Melts. *Proc. Natl. Acad. Sci. U. S. A.* 2018, 115, 847–854. https://doi.org/10.1073/pnas.1717850115.
- (66) Jeon, S.; Jun, T.; Jo, S.; Ahn, H.; Lee, S.; Lee, B.; Ryu, D. Y. Frank–Kasper Phases Identified in PDMS- b -PTFEA Copolymers with High Conformational Asymmetry. *Macromol. Rapid Commun.* **2019**, *40*, 1900259. https://doi.org/10.1002/marc.201900259.
- (67) Ndoni, S.; Papadakis, C. M.; Bates, F. S.; Almdal, K. Laboratory-Scale Setup for Anionic Polymerization under Inert Atmosphere. *Rev. Sci. Instrum.* **1995**, *66*, 1090–1095. https://doi.org/10.1063/1.1146052.
- (68) Brandrup, J.; Immergut, E. H.; Grulke, E. A. *Polymer Handbook*; Wiley-Interescience: New York, 1999.
- (69) Medrano, R.; Laguna, M. T. R.; Saiz, E.; Tarazona, M. P. Analysis of Copolymers of Styrene and Methyl Methacrylate Using Size Exclusion Chromatography with Multiple Detection. *Phys. Chem. Chem. Phys.* **2003**, *5*, 151–157. https://doi.org/10.1039/b205461b.
- (70) Richardson, M. J.; Savill, N. G. Volumetric Properties of Polystyrene: Influence of Temperature, Molecular Weight and Thermal Treatment. *Polymer* **1977**, *18*, 3–9. https://doi.org/10.1016/0032-3861(77)90253-1.
- (71) Fetters, L. J.; Lohse, D. J.; Richter, D.; Witten, T. A.; Zirkel, A. Connection between Polymer Molecular Weight, Density, Chain Dimensions, and Melt Viscoelastic Properties. *Macromolecules* **1994**, *27*, 4639–4647. https://doi.org/10.1021/ma00095a001.
- (72) Kato, K. Die Elektronenmikroskopischen Darstellungen von ABS-Kunststoffen. *Kolloid-Zeitschrift Zeitschrift für Polym.* **1967**, *220*, 24–31. https://doi.org/10.1007/BF02086053.

- (73) Arora, A.; Qin, J.; Morse, D. C.; Delaney, K. T.; Fredrickson, G. H.; Bates, F. S.; Dorfman, K. D. Broadly Accessible Self-Consistent Field Theory for Block Polymer Materials Discovery. *Macromolecules* **2016**, 49, 4675–4690. https://doi.org/10.1021/acs.macromol.6b00107.
- (74) Arora, A.; Morse, D. C.; Bates, F. S.; Dorfman, K. D. Accelerating Self-Consistent Field Theory of Block Polymers in a Variable Unit Cell. *J. Chem. Phys.* **2017**, *146*, 244902. https://doi.org/10.1063/1.4986643.
- (75) Matsen, M. W. Phase Behavior of Block Copolymer/Homopolymer Blends. *Macromolecules* **1995**, *28*, 5765–5773.
- (76) Friauf, J. B. Crystal Structure of Magnesium Di-Zincide. *Phys. Rev.* **1927**, *29*, 34–40.
- (77) Laves, F.; Löhberg, K. Die Kristallstruktur von Intermetallischen Verbindungen Der Formel AB₂. *Nachr. Ges. Wiss. Göttingen, Math-phys. Kl. Neue Folge* **1934**, *1*, 59–66.
- (78) Laves, F.; Witte, H. Die Kristallstruktur Des MgNi₂ Und Seine Beziehungen Zu Den Typen Des MgCu₂ Und MgZn₂. *Metallwirtschaft* **1935**, *14*, 645–649.
- (79) Lindsay, A. P.; Jayaraman, A.; Peterson, A. J.; Mueller, A. J.; Weigand, S.; Mahanthappa, M. K.; Lodge, T. P.; Bates, F. S. Reevaluation of Poly(Ethylene- Alt -Propylene)- Block Polydimethylsiloxane Phase Behavior Uncovers Topological Close-Packing and Epitaxial Quasicrystal Growth. *ACS Nano* **2021**, *ASAP Article*. https://doi.org/10.1021/acsnano.1c02420.
- (80) Feng, X.; Liu, G.; Guo, D.; Lang, K.; Zhang, R.; Huang, J.; Su, Z.; Li, Y.; Huang, M.; Li, T.; et al. Transition Kinetics of Self-Assembled Supramolecular Dodecagonal Quasicrystal and Frank-Kasper σ Phases in AB_n Dendron-Like Giant Molecules. *ACS Macro Lett.* **2019**, *8*, 875–881. https://doi.org/10.1021/acsmacrolett.9b00287.
- (81) Lee, S.; Gillard, T. M.; Bates, F. S. Fluctuations, Order, and Disorder in Short Diblock Copolymers. *AIChE J.* **2013**, *59*, 3502–3513. https://doi.org/10.1002/aic.
- (82) Lee, S. Structure and Dynamics of Block Copolymer Based Soft Materials. *Ph.D. Thesis*, University of Minnesota, 2011.
- (83) Chen, L.; Lee, H. S.; Lee, S. Close-Packed Block Copolymer Micelles Induced by Temperature Quenching. *Proc. Natl. Acad. Sci. U. S. A.* **2018**, *115*, 7218–7223. https://doi.org/10.1073/pnas.1801682115.
- (84) Lynd, N. A.; Hillmyer, M. A. Influence of Polydispersity on the Self-Assembly of Diblock Copolymers. *Macromolecules* **2005**, *38*, 8803–8810. https://doi.org/10.1021/ma051025r.
- (85) Cooke, D. M.; Shi, A. C. Effects of Polydispersity on Phase Behavior of Diblock Copolymers. *Macromolecules* **2006**, *39*, 6661–6671. https://doi.org/10.1021/ma060717s.
- (86) Hashimoto, T.; Yamasaki, K.; Koizumi, S.; Hasegawa, H. Ordered Structure in Blends of Block Copolymers. 1. Miscibility Criterion for Lamellar Block Copolymers. *Macromolecules* **1993**, *26*, 2895–2904. https://doi.org/10.1021/ma00063a039.

- (87) Hashimoto, T.; Koizumi, S.; Hasegawa, H. Ordered Structure in Blends of Block Copolymers. 2. Self-Assembly for Immiscible Lamella-Forming Copolymers. *Macromolecules* **1994**, *27*, 1562–1570. https://doi.org/10.1021/ma00084a043.
- (88) Koizumi, S.; Hasegawa, H.; Hashimoto, T. Ordered Structure in Blends of Block Copolymers. 3. Self-Assembly in Blends of Sphere- or Cylinder-Forming Copolymers. *Macromolecules* **1994**, *27*, 4371–4381. https://doi.org/10.1021/ma00093a044.
- (89) Jayaraman, A.; Zhang, D. Y.; Dewing, B. L.; Mahanthappa, M. K. Path-Dependent Preparation of Complex Micelle Packings of a Hydrated Diblock Oligomer. *ACS Cent. Sci.* **2019**, *5*, 619–628. https://doi.org/10.1021/acscentsci.8b00903.
- (90) Jayaraman, A.; Mahanthappa, M. K. Counterion-Dependent Access to Low-Symmetry Lyotropic Sphere Packings of Ionic Surfactant Micelles. *Langmuir* **2018**, *34*, 2290–2301. https://doi.org/10.1021/acs.langmuir.7b03833.
- (91) Matsen, M. W.; Bates, F. S. One-Component Approximation for Binary Diblock Copolymer Blends. *Macromolecules* **1995**, *28*, 7298–7300. https://doi.org/10.1021/ma00125a041.
- (92) Willis, J. D.; Beardsley, T. M.; Matsen, M. W. Simple and Accurate Calibration of the Flory-Huggins Interaction Parameter. *Macromolecules* **2020**, *53*, 9973–9982. https://doi.org/10.1021/acs.macromol.0c02115.
- (93) Grason, G. M. The Packing of Soft Materials: Molecular Asymmetry, Geometric Frustration and Optimal Lattices in Block Copolymer Melts. *Phys. Rep.* **2006**, *433*, 1–64. https://doi.org/10.1016/j.physrep.2006.08.001.
- (94) Lodge, T. P.; Pudil, B.; Hanley, K. J. The Full Phase Behavior for Block Copolymers in Solvents of Varying Selectivity. *Macromolecules* **2002**, *35*, 4707–4717. https://doi.org/10.1021/ma0200975.
- (95) Hamley, I. W.; Daniel, C.; Mingvanish, W.; Mai, S. M.; Booth, C.; Messe, L.; Ryan, A. J. From Hard Spheres to Soft Spheres: The Effect of Copolymer Composition on the Structure of Micellar Cubic Phases Formed by Diblock Copolymers in Aqueous Solution. *Langmuir* **2000**, *16*, 2508–2514. https://doi.org/10.1021/la991035j.
- (96) Huang, Y. Y.; Hsu, J. Y.; Chen, H. L.; Hashimoto, T. Precursor-Driven Bcc-Fcc Order-Order Transition of Sphere-Forming Block Copolymer/Homopolymer Blend. *Macromolecules* **2007**, *40*, 3700–3707. https://doi.org/10.1021/ma070066f.
- (97) Mahynski, N. A.; Kumar, S. K.; Panagiotopoulos, A. Z. Relative Stability of the FCC and HCP Polymorphs with Interacting Polymers. *Soft Matter* **2015**, *11*, 280–289. https://doi.org/10.1039/c4sm02191f.

Supporting Information

Complex Phase Formation in Particle-Forming AB/AB' Diblock Copolymer Blends with Variable Core Block Lengths

Aaron P. Lindsay,¹ Guo Kang Cheong,¹ Austin J. Peterson,¹ Steven Weigand,³ Kevin D. Dorfman,¹ Timothy P. Lodge,^{1,2} Frank S. Bates*¹

¹Department of Chemical Engineering and Materials Science and ²Department of Chemistry, University of Minnesota, Minneapolis, MN 55455, USA

³DND-CAT Synchrotron Research Center, Northwestern University, APS/ANL Building 432-A004, 9700 South Cass Ave, Argonne, Illinois 60439, USA

*Corresponding Author: Frank S. Bates (bates001@umn.edu)

Contents	Page
Figure S1. SEC data	S3
Figure S2. Extended 1D SAXS trace for C14 Laves phase in a SB1/SB2 blend	S3
Table S1. Indexing and residuals for C14 Laves phase in a SB1/SB2 blend	S4
Table S2. Indexing and residuals for σ phase in a SB3/SB4 blend	S5
Figure S3. 1D SAXS trace for a SB3/SB4 blend with $\phi_2 = 0.80$ at 180 °C	S 6
Figure S4. SAXS data collected for SB3/SB5 blends at 120 °C	S6
Figure S5. 1D SAXS traces collected for SB3/SB5 blends with $\phi_2 = 0.31$	S 7
Figure S6. TEM micrograph collected from a SB3/SB5 blend with $\phi_2 = 0.31$	S 8
Figure S7. 1D SAXS trace for a HCP phase in a SB3/SB5 blend	S9
Figure S8 1D SAXS trace for a σ/HCP coexistence in a SB3/SB5 blend	S9
Table S3. Indexing and residuals for a σ/HCP coexistence in a SB3/SB5 blend	S10
Figure S9 1D SAXS trace for an A15/σ coexistence in a SB3/SB5 blend	S11
Table S4. Indexing and residuals for an A15/ σ coexistence in a SB3/SB5 blend	S12
Table S5. Indexing and residuals for a QC in a SB3/SB5 blend	S13
Table S6. Indexing and residuals for an A15/HEX _C coexistence in a SB3/SB5 blend	S13
Calculation of mean particle radii	S14
Dispersity	S17
Self-consistent mean field theory (SCFT)	S19
Figure S10. Free energy profiles as a function of composition	S20
Figure S11. Free energy profiles as a function of χN	S20
Figure S12. SCFT phase portrait at increased χN	S21
Figure S13. SCFT-derived composition maps for the σ and A15 phases	S22
References	S23

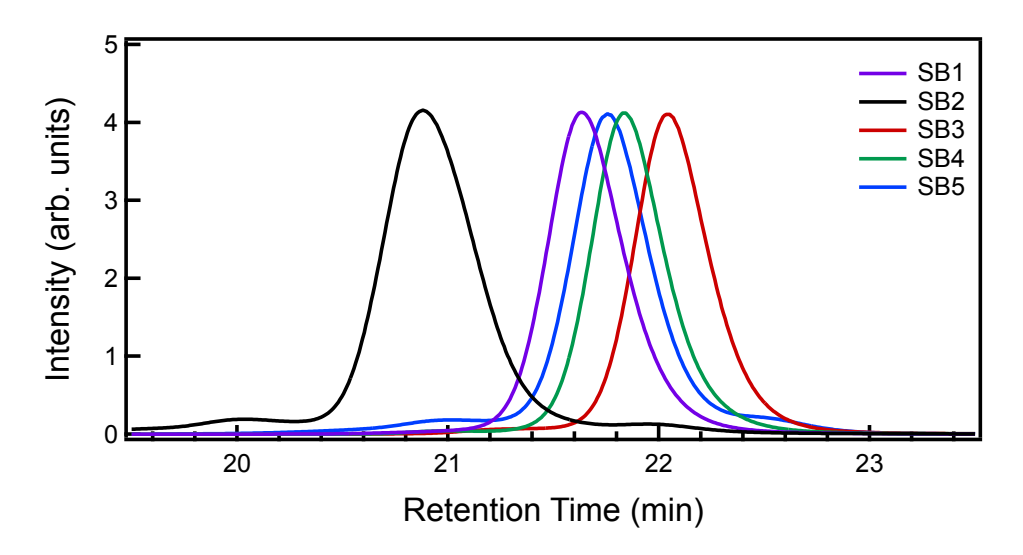


Figure S1. Size exclusion chromatography light scattering traces collected in tetrahydrofuran.

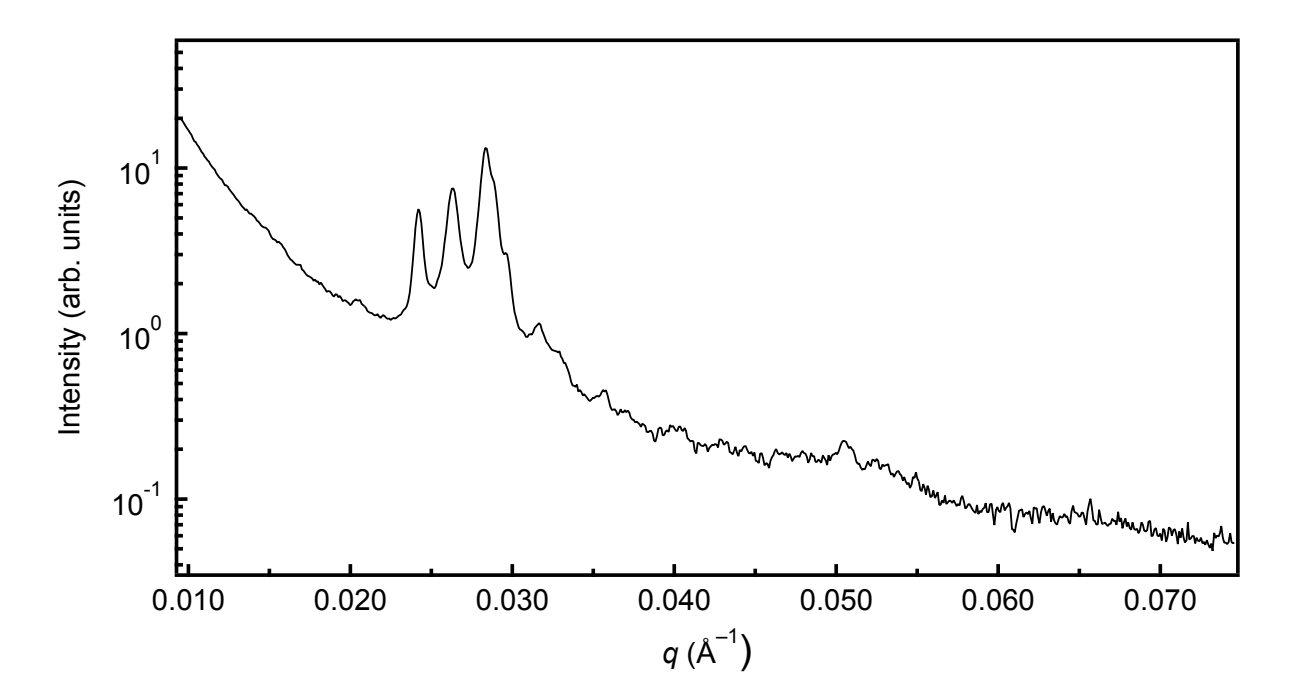


Figure S2. Extended 1D SAXS trace for the C14 Laves phase observed in SB1/SB2 blends with $\phi_2 = 0.075$ at 150 °C following the thermal processing outlined in Figure 2 and the main text. Indexing and residuals can be found in Table S1.

Table S1. Observed and calculated peak positions for the C14 Laves phase in Figures 2 and S2; data were collected from SB1/SB2 blends with $\phi_2 = 0.075$ at 150 °C. Peak positions were calculated as $q_{\rm hkl} = 2\pi \left[(4/3) \left(h^2 + hk + k^2 \right) / a^2 + l^2 / c^2 \right]^{1/2}$ based on $P6_3/mmc$ space group symmetry with lattice parameters a = 520.0 Å and c = 847.5 Å.

Miller Indices (hkl)	$q_{ m obs} \ (1/ m \AA)$	<i>q</i> _{calc} (1/Å)	% Residual $(\Delta q/q_{\rm calc} \times 100)$
(100)	0.013948	0.013952	0.03
(002)	0.014846	0.014827	-0.13
(101)	0.015744	0.015800	0.35
(102)	0.020325	0.020359	0.17
(110)	0.024188	0.024166	-0.09
(103)	0.026292	0.026254	-0.14
(200)	_	0.027905	_
(112)	0.028319	0.028352	0.12
(201)	0.028858	0.028873	0.05
(004)	0.029577	0.029653	0.26
(202)	0.031643	0.031599	-0.14
(104)	0.032900	0.032772	-0.39
(203)	0.035685	0.035683	-0.01
(210)	0.036942	0.036914	-0.07

Table S2. Observed and calculated peak positions for the σ phase coexisting with HEX_C in Figures 3 and 4. Data were collected from an SB3/SB4 blend with $\phi_2 = 0.80$ at 150 °C. Peak positions were calculated as $q_{\rm hkl} = 2\pi \left[(h^2 + hk + k^2)/a^2 + l^2/c^2 \right]^{1/2}$ based on $P4_2/mnm$ space group symmetry with lattice parameters a = 917.8 Å and c = 484.9 Å.

Miller Indices	$q_{ m obs}$	$q_{ m calc}$	% Residual
(hkl)	(1/Å)	(1/Å)	$(\Delta q/q_{\rm calc} \times 100)$
(110)	_	0.009682	_
(200)	_	0.013692	_
(101)	_	0.014654	_
(210)	_	0.015308	_
(111)	_	0.016174	_
(220)	_	0.019363	_
(211)	0.020048	0.020055	0.04
(310)	0.021753	0.021649	-0.48
(221)	0.023369	0.023298	-0.30
(301)	0.024267	0.024283	0.07
(320)	0.024626	0.024684	0.23
(311)	0.025255	0.025230	-0.10
(002)	0.025917	0.025913	-0.02
(400)	0.027320	0.027384	0.23
(112)	_	0.027663	_
(321)	0.027858	0.027877	0.07
(410)	0.028217	0.028227	0.03
(330)	0.029025	0.029045	0.07
(202)	0.029295	0.029308	0.04
(212)	_	0.030097	_
(420)	_	0.030616	_
(411)	0.03109	0.031058	-0.10
(331)	0.031809	0.031804	-0.02
(222)	0.032347	0.032348	0.00
(421)	0.033155	0.033245	0.27
(312)	0.033694	0.033766	0.21
(430)	_	0.034230	_
(510)	_	0.034908	_
(322)	0.035849	0.035788	-0.17
(501)	0.036657	0.036600	-0.16
(520)	_	0.036867	_
(511)	0.037195	0.037235	0.11

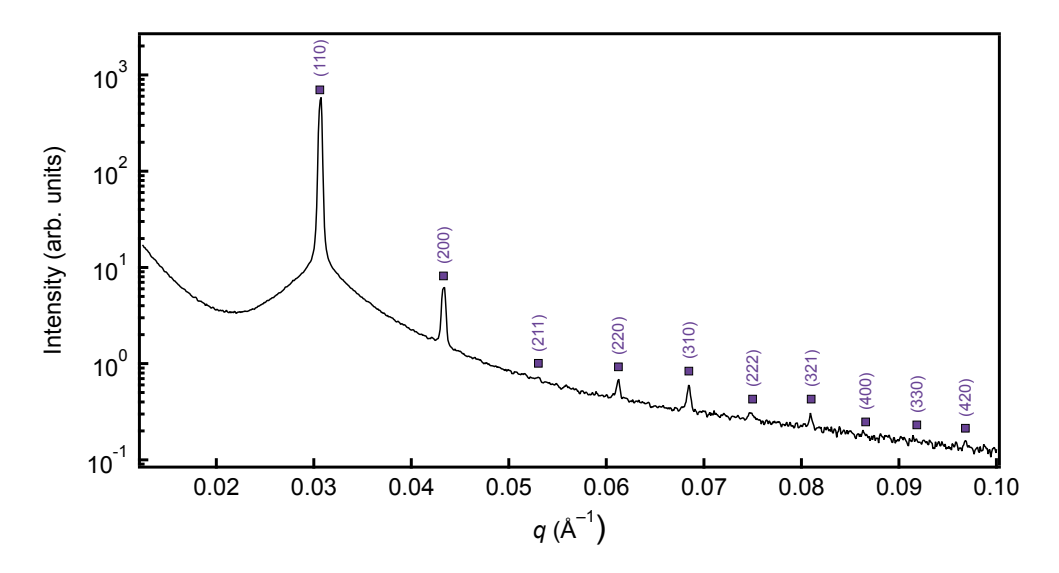


Figure S3. 1D SAXS trace collected from a SB3/SB4 blend with $\phi_2 = 0.80$ following a 169 h anneal at 180 °C. The trace is indexed to a BCC phase.

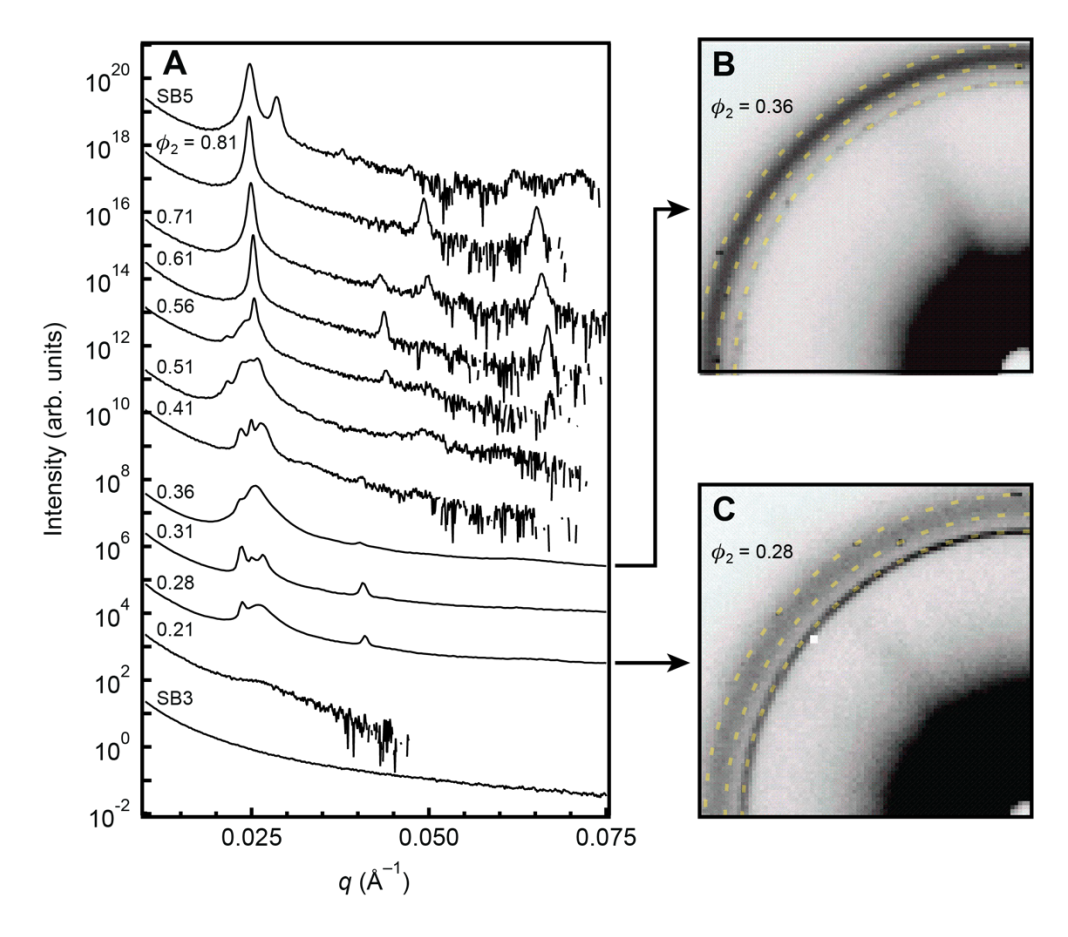


Figure S4. (A) 1D and (B,C) 2D SAXS data collected from SB3/SB5 blends following extended annealing (66-92 h) at 120 °C. 2D SAXS data in B and C was collected following 92 h of annealing at 120 °C. 2D data is indexed to the HCP phase (yellow dashed lines).

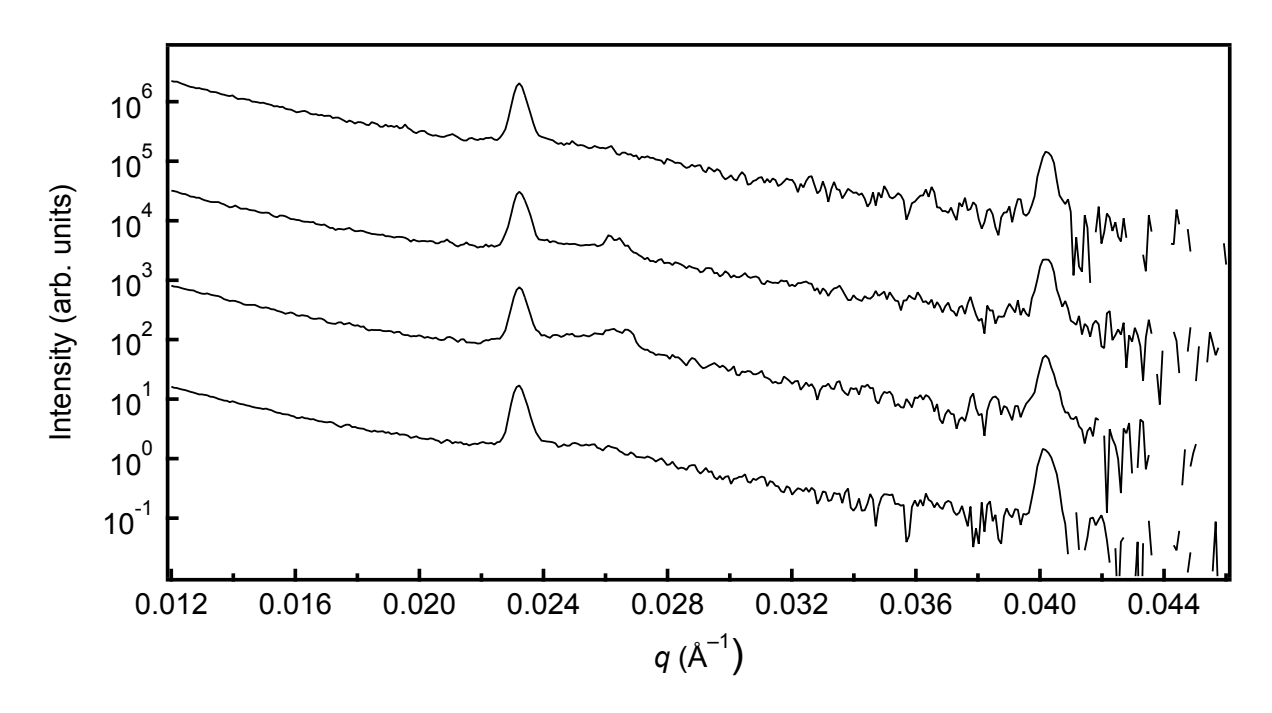


Figure S5. 1D SAXS traces collected from different locations on a SB3/SB5 blend with $\phi_2 = 0.31$ following 66 h of annealing at 150 °C.

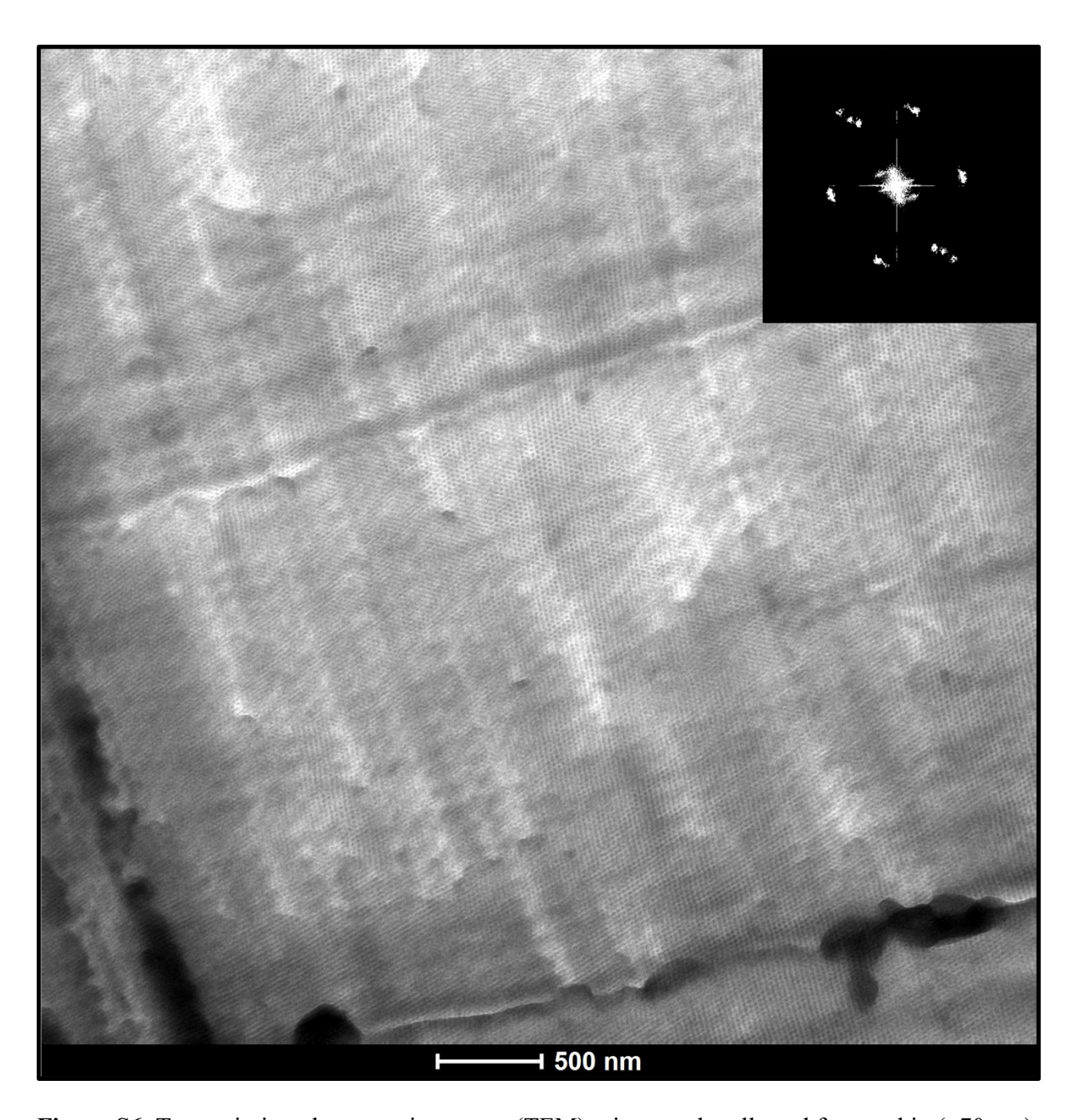


Figure S6. Transmission electron microscopy (TEM) micrograph collected from a thin (\sim 70 nm) microtomed section of a SB3/SB5 blend with $\phi_2 = 0.31$. Prior to microtoming, the sample was annealed for 66 h at 150 °C, after which the SAXS patterns in Figures 5A,C and S5 were collected and the sample was vitrified in liquid nitrogen. The inset in the upper right corner is a Fourier transform of the image displaying the 6-fold rotation symmetry present over large areas.

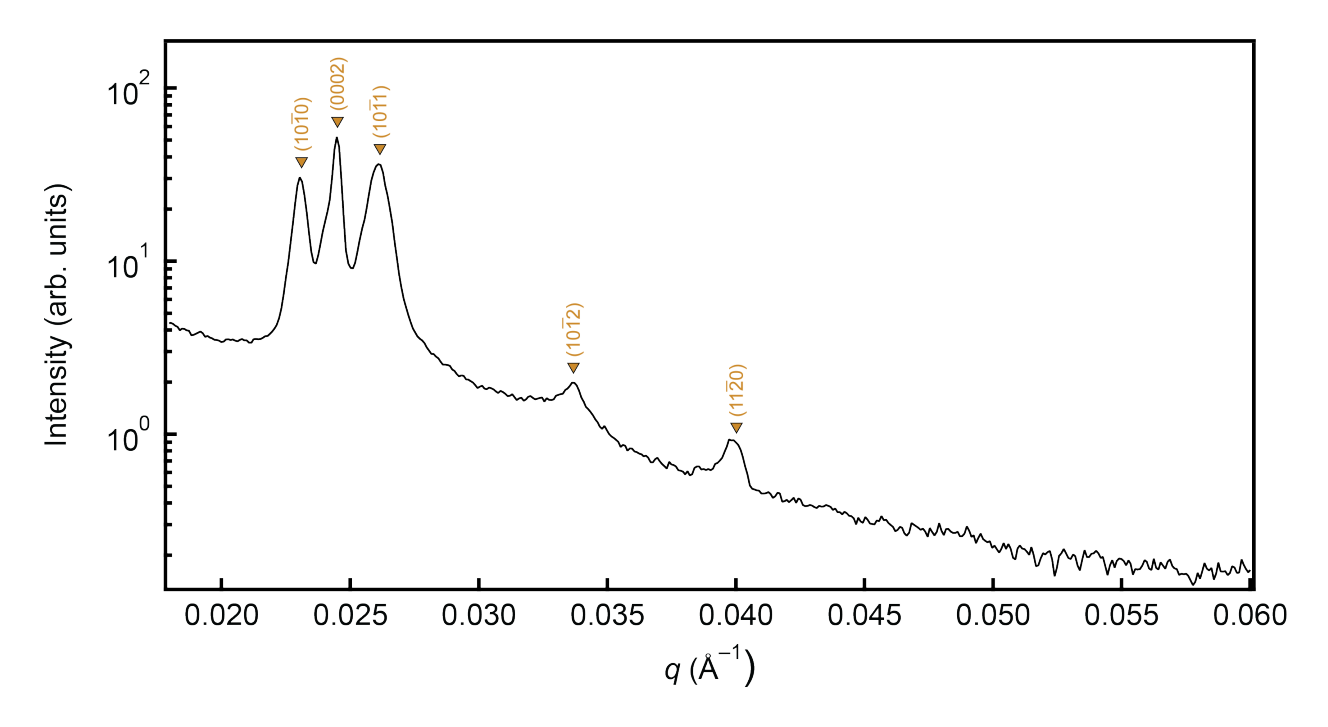


Figure S7. 1D SAXS trace collected from a SB3/SB5 blend with $\phi_2 = 0.41$ following 92 h of annealing a 180 °C. The trace is indexed to a HCP phase. Additional patterns can be found in Figures 5 and S9. Indexing and residuals can be found in Table S4.

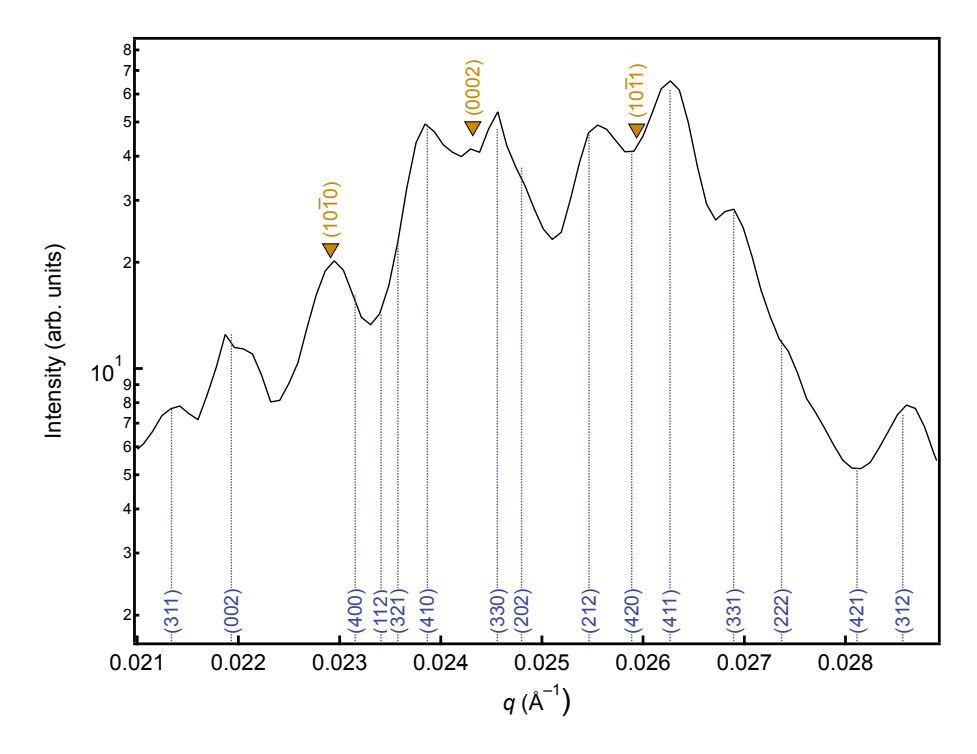


Figure S8. 1D SAXS trace collected from a SB3/SB5 blend with $\phi_2 = 0.46$ after annealing at 180 °C for 66 h. Lines and inverted triangles denote peaks associated with the σ and HCP phases, respectively. Indexing and residuals can be found in Table S3.

Table S3. Observed and calculated peak positions for the σ/HCP phase coexistence evidenced in Figures 5 and S10; data were collected from SB3/SB5 blends with $\phi_2 = 0.46$ at 180 °C. Peak positions for the HCP phase were calculated as $q_{\rm hkl} = 2\pi \left[(4/3) \left(h^2 + hk + k^2 \right) / a^2 + l^2 / c^2 \right]^{1/2}$ based on $P6_3/mmc$ space group symmetry with lattice parameters a = 316.7 Å and c = 517.1 Å. Peak positions for the σ phase were calculated as $q_{\rm hkl} = 2\pi \left[(h^2 + k^2)/a^2 + l^2/c^2 \right]^{1/2}$ based on $P4_2/mnm$ space group symmetry with lattice parameters a = 1085.5 Å and c = 573.0 Å.

Miller Indices (hkil) or (hkl)	$q_{ m obs} \ m (1/\AA)$	$q_{ m calc} \ (1/{ m \AA})$	% Residual $(\Delta q/q_{\rm calc} \times 100)$
(*****) ***		CP	(<u>-</u> 4. 4 care)
(1010)	0.022946	0.022910	-0.16
(0002)	0.024293	0.024300	0.03
$(10\overline{1}1)$	_	0.025933	-0.26
$(10\overline{1}2)$	0.033539	0.033397	-0.43
$(11\bar{2}0)$	0.039643	0.039682	0.10
$(10\overline{1}3)$	_	0.043052	_
$(20\overline{2}0)$	0.046016	0.045820	-0.43
$(11\bar{2}2)$	0.046555	0.046531	-0.05
$(20\bar{2}1)$	0.047363	0.047404	0.09
(0004)	0.048799	0.048599	-0.41
$(20\overline{2}2)$	0.051761	0.051865	0.20
	(<u> </u>	
(211)	0.016932	0.016964	0.19
(310)	0.018279	0.018304	0.14
(221)	0.019625	0.019705	0.40
(301)	0.020613	0.020537	-0.37
(320)	_	0.020870	_
(311)	0.021331	0.021337	0.03
(002)	0.021959	0.021931	-0.13
(400)	_	0.023153	_
(112)	_	0.023409	_
(321)	_	0.023575	_
(410)	0.023844	0.023866	0.09
(330)	0.024562	0.024558	-0.02
(202)	0.024832	0.024799	-0.13
(212)	0.02555	0.025465	-0.33
(420)	_	0.025886	_
(411)	0.026268	0.026264	-0.01
(331)	0.026896	0.026895	-0.01

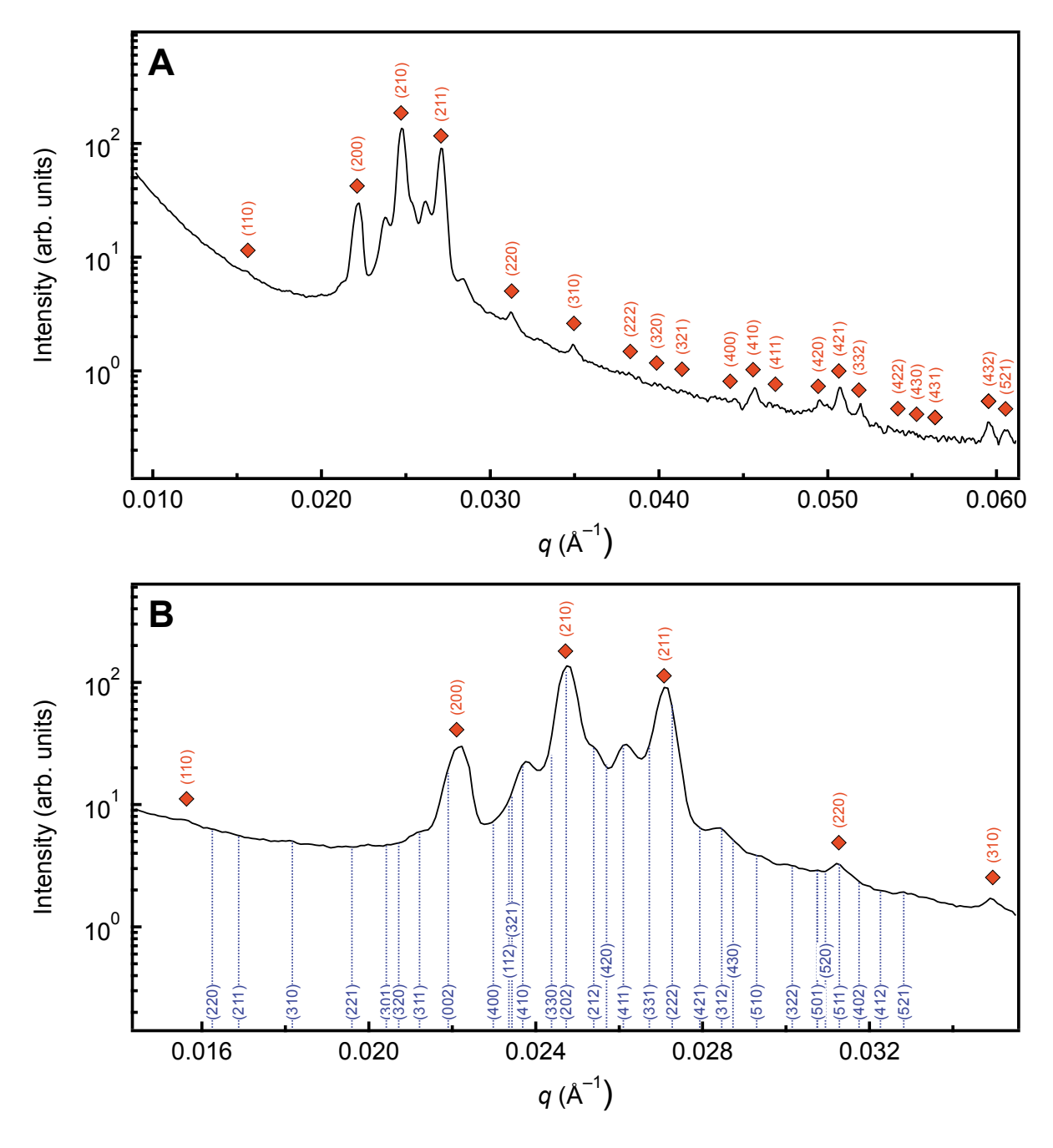


Figure S9. 1D SAXS trace collected from a SB3/SB5 blend with $\phi_2 = 0.51$ after annealing at 180 °C for 66 h. Lines and diamonds denote peaks associated with σ and A15 phases, respectively. Indexing and residuals can be found in Table S6.

Table S4. Observed and calculated peak positions for the A15/σ phase coexistence evidenced in Figures 5 and S11; data were collected from SB3/SB5 blends with $\phi_2 = 0.51$ at 180 °C. Peak positions for the A15 phase were calculated as $q_{\rm hkl} = 2\pi \left[(h^2 + k^2 + l^2)/a^2 \right]^{1/2}$ based on $Pm\bar{3}n$ space group symmetry with a lattice parameter of a = 568.5 Å. Peak positions for the σ phase were calculated as $q_{\rm hkl} = 2\pi \left[(h^2 + k^2)/a^2 + l^2/c^2 \right]^{1/2}$ based on $P4_2/mnm$ space group symmetry with lattice parameters a = 1093.3 Å and c = 573.7 Å.

Miller Indices (hkl)	$q_{ m obs} \ (1/ m \AA)$	$q_{ m calc} \ (1/{ m \AA})$	% Residual $(\Delta q/q_{\rm calc} \times 100)$
	A	15	
(110)	0.015586	0.015630	0.28
(200)	0.022228	0.022104	-0.56
(210)	0.024742	0.024713	-0.12
(211)	0.027165	0.027072	-0.34
(220)	0.031205	0.031260	0.18
(310)	0.034885	0.034950	0.19
(222)	0.038207	0.038285	0.20
(320)	0.039733	0.039849	0.29
(321)	0.041348	0.041353	0.01
(400)	0.0444	0.044208	-0.43
(410)	0.045657	0.045569	-0.19
(411)	0.047004	0.046890	-0.24
(420)	0.049517	0.049426	-0.18
(421)	0.050684	0.050647	-0.07
(332)	0.051941	0.051839	-0.20
	(5	
(410)	0.023754	0.023695	-0.25
(330)	_	0.024382	_
(202)	_	0.024735	_
(212)	0.02546	0.025394	-0.26
(420)	_	0.025701	_
(411)	0.026178	0.026103	-0.29
(331)	_	0.026728	_
(222)	_	0.027275	_
(421)	_	0.027937	_
(312)	0.028422	0.028460	0.13
(430)	_	0.028734	_
(510)	0.02941	0.029303	-0.36
(322)	0.030038	0.030150	0.37

Table S5. Observed and calculated peak positions for the QC evidenced in Figures 5 and S12; data were collected from SB3/SB5 blends with $\phi_2 = 0.51$ at 150 °C. Peak positions were calculated as described by Iwami and Ishimasa [1] based on a $P12_6/mmc$ space group symmetry, a tiling edge length a = 572.9 Å, and a periodicity of c = 575.6 Å.

Miller Indices	$q_{ m obs}$	$q_{ m calc}$	% Residual
$(a_1 a_2 a_3 a_4 a_5)$	(1/Å)	(1/Å)	$(\Delta q/q_{\rm calc} \times 100)$
(11000)	_	0.012233	_
(00002)	0.021780	0.021832	0.24
(12100)	0.023844	0.023633	-0.89
(01102)	0.024921	0.025026	0.42
$(220\overline{1}1)$	0.025999	0.026032	0.13
(11102)	0.028063	0.027856	-0.74
(12202)	_	0.036531	_
(00004)	0.043664	0.043664	0.00
(01104)	0.045298	0.045345	0.10

Table S6. Observed and calculated peak positions for the A15 phase coexisting with HEX_C evidenced in Figures 5 and S13; data was collected from SB3/SB5 blends with $\phi_2 = 0.56$ at 180 °C. Peak positions for the A15 phase were calculated as $q_{hkl} = 2\pi \left[(h^2 + k^2 + l^2)/a^2 \right]^{1/2}$ based on $Pm\overline{3}n$ space group symmetry with a lattice parameter of a = 577.0 Å.

Miller Indices (hkl)	$q_{ m obs} \ (1/ m \AA)$	$q_{ m calc} \ (1/{ m \AA})$	% Residual $(\Delta q/q_{\rm calc} \times 100)$
(110)	_	0.015400	_
(200)	0.021753	0.021779	0.12
(210)	0.024357	0.024349	-0.03
(211)	0.026601	0.026673	0.27
(220)	_	0.030800	_

Calculation of mean particle radii:

For a periodic particle packing, the mean particle radius $\langle R \rangle$ can be calculated as:

$$\langle R \rangle = \left(\frac{3V_{\rm UC}}{4\pi\rho_{\rm P,UC}}\right)^{1/3} \tag{S1}$$

where $V_{\rm UC}$ is the unit cell volume, which can be readily determined *via* SAXS, and $\rho_{\rm P,UC}$ is the number of particles per unit cell set by the packing. In the most general form, unit cell volume can be calculated as:

$$V_{\rm UC} = a b c \left(1 - \cos^2 \alpha - \cos^2 \beta - \cos^2 \gamma + 2 \cos \alpha \cos \beta \cos \gamma\right)^{1/2}$$
 (S2)

where a, b, and c are lattice constants and the angles a, β , and γ are lattice parameters. These values are determined from SAXS from the relations:

$$q_{\text{hkl,cubic}} = 2\pi \left(\frac{\left(h^2 + k^2 + l^2\right)}{a^2}\right)^{1/2}$$
 (S3)

$$q_{\text{hkl,hexagonal}} = 2\pi \left(\frac{4(h^2 + hk + k^2)}{3a^2} + \frac{l^2}{c^2} \right)^{1/2}$$
 (S4)

$$q_{\text{hkl,tetragonal}} = 2\pi \left(\frac{(h^2 + k^2)}{a^2} + \frac{l^2}{c^2} \right)^{1/2}$$
 (S5)

for cubic, hexagonal, or tetragonal lattices, where q_{hkl} is the scattering wavevector for plane (hkl), $\alpha = \beta = \gamma = 90^{\circ}$ for a cubic or tetragonal lattice, and $\alpha = \beta = 90^{\circ}$ and $\gamma = 120^{\circ}$ for a hexagonal lattice.

From these relations, $\langle R \rangle$ can be calculated for the phases observed in this work as:

$$\langle R \rangle_{\text{BCC}} = R_{\text{BCC}} = \frac{3^{1/3} 2^{1/2} \pi^{2/3}}{q_{110}}$$
 (S6)

$$\langle R \rangle_{\text{FCC}} = R_{\text{FCC}} = \frac{3^{5/6} \pi^{2/3}}{2^{1/3} q_{111}}$$
 (S7)

$$\langle R \rangle_{\text{HCP}} = R_{\text{HCP}} = \frac{2^{2/3} \pi^{2/3} (c/a)^{1/3}}{q_{10\overline{1}0}}$$
 (S8)

$$\langle R \rangle_{\sigma} = \frac{2\pi^{2/3}}{5^{1/3} (c/a)^{2/3} q_{002}}$$
 (S9)

$$\langle R \rangle_{A15} = \frac{3^{1/3} \pi^{2/3}}{2^{1/6} q_{110}}$$
 (S10)

$$\langle R \rangle_{\rm C14} = \frac{2^{1/3} \pi^{2/3} (c/a)^{1/3}}{3^{1/3} q_{10\bar{1}0}}$$
 (S11)

Owing to a lack of translational symmetry, $\langle R \rangle$ for a dodecagonal quasicrystal (QC) or a liquidlike packing (LLP) can only be estimated. For a QC, this is best done by taking the (00002) reflection as the σ q_{002} peak owing to the close structural relationship between the two phases and the invariance of this reflection on transition to the σ phase.^{2,3} For LLP the principal reflection can be taken as the q_{110} peak of the BCC phase by a similar argument. On calculating $\langle R \rangle$, the core radius can be calculated as:

$$\langle R_{\text{core}} \rangle = f_{\text{core}}^{-1/3} \langle R \rangle$$
 (S12)

where f_{core} is volume fraction of the core domain assuming complete segregation of both blocks. This core radius can then be used to calculate the underlying spherical form factor.

A similar strategy can be used to calculate the radius of cylinders in the hexagonally-packed cylinder (HEX_C) phase. However, the functional form changes slightly owing to periodicity in only two dimensions. $\langle R \rangle$ is instead calculated as:

$$R_{\rm cyl} = \left(\frac{A_{\rm UC}}{\pi \rho_{\rm C,UC}}\right)^{1/2} \tag{S13}$$

where $A_{\rm UC}$ is the unit cell area, which can be readily determined *via* SAXS, and $\rho_{\rm C,UC}=1$ is the number of cylinders per unit cell. The unit cell area can be calculated as:

$$A_{\rm UC} = \frac{3^{1/2}a^2}{2} \tag{S14}$$

The lattice parameter *a* is determined from SAXS according to the relation:

$$q_{\text{hk,hexagonal2D}} = 2\pi \left(\frac{4(h^2 + hk + k^2)}{3a^2} \right)^{1/2}$$
 (S15)

From these equations, $\langle R \rangle$ can be calculated for the HEX_C phase as:

$$R_{\rm cyl} = \frac{2^{3/2} \pi^{1/2}}{3^{1/4} q_{10}} \tag{S16}$$

On calculating $R_{\rm cyl}$, the cylinder core radius can then be calculated as:

$$R_{\text{core,cyl}} = f_{\text{core}}^{1/2} R_{\text{cyl}}$$
 (S17)

where f_{core} is again the volume fraction of the core domain assuming complete segregation of both blocks. This core radius can then be used to calculate the underlying cylindrical form factor.

Dispersity:

Core block dispersity $D \approx 1.12$ was estimated for SB3/SB4 blends with $\phi_2 = 0.80$ approximating the constituent diblock copolymers as monodisperse via the relation:

$$D = \frac{M_{\rm w}}{M_{\rm n}} \tag{S18}$$

where $M_{\rm w}$ and $M_{\rm n}$ are the weight- and number-average block molecular weights calculated as:

$$M_{\rm n} = x_1 M_{\rm n,1} + x_2 M_{\rm n,2} \tag{S19}$$

$$M_{\rm w} = \frac{x_1 M_{\rm n,1}^2 + x_2 M_{\rm n,2}^2}{x_1 M_{\rm n,1} + x_2 M_{\rm n,2}}$$
 (S20)

where values of M_n for each block and polymer can be found in Table S1 and x_i is the mole fraction of copolymer i in the core domain. A similar approach can be used to estimate the dispersity of the corona as $D \approx 1.001$. Notably, this approach only provides an estimate and neglects the dispersity of each polymer, each determined via size exclusion chromatography (SEC) to be $D \approx 1.01$.

To compare this value with previously investigated 1,4-polyisoprene-*block*-poly(\pm -lactide) (IL) diblock copolymers, we assume a I precursor dispersity of 1.06, a reasonable estimate for low molecular weight I synthesized *via* anionic polymerization,⁴ and independent block dispersities. Using the rule for the sum of variances of statistical distributions (*i.e.*, $D_{PIPLA} = w_{PI}^2(D_{PI} - 1) + w_{PLA}^2(D_{PLA} - 1) + 1$, where w_i is the mass fraction of block i), it can be found that many of the σ -forming IL diblock copolymers reported in the literature likely had core (L) block dispersities greater than the $D_{core} = 1.2$ we found in this work to be sufficient to drive σ -formation. ⁵⁻¹² It should be noted that the accuracy of such calculations is limited by that of the assumed I precursor dispersity and the resolution of the instruments used for dispersity measurements. ¹³ However, there are several reasons one might anticipate a higher dispersity for the second block. First, ring-opening polymerization of lactides generally results in higher dispersity (~1.1–2.0) than anionic polymerization of isoprene (< 1.1). ^{5,14,15} Second, it is anticipated that some fraction of PI precursor will be present in the final diblock copolymer due to a combination of early termination,

incomplete reinitiation, and challenges inherent to purification.¹³ Third, when considering the low molecular weight of these polymers, generally characterized by an average block length of 45 isoprene and 6 lactide monomer units, it is clear that the loss or gain of only a few lactide monomer units over the course of the polymerization would have a dramatic effect on the block dispersity.

Self-consistent mean-field theory (SCFT):

Calculations based on self-consistent mean-field theory were performed using the open-source Polymer Self-Consistent Field software package (PSCF). We performed binary blend canonical ensemble calculations at $N_2/N_1 = 1.4$, $N_{B,1} = N_{B,2}$, $f_{A,1} = 0.12$, $f_{A,2} = 0.38$ and a conformational asymmetry of $\varepsilon = b_B/b_S$ (v_S/v_B) = 1.7. Note this differs modestly from experiments, where $f_{A,2}$ = 0.388, but is within experimental error and, thus, has a negligible impact on the applicability of the calculations to the experimental results. We scanned a range of χN (20–30) and ϕ_2 (0–1), mimicking the parameter space explored experimentally. The candidate phases tested in the canonical ensemble calculations include the body-centered cubic (BCC), face-centered cubic (FCC), hexagonally close-packed (HCP), hexagonally-packed cylinder (HEX_C), double gyroid (GYR), and disordered (DIS) phases as well as the Frank-Kasper (FK) σ, A15, C14, and C15 phases. SCFT calculations were performed using a grid size of 64×64×64 for the three-dimensional structures except for the σ and two-dimensional HEX_C phases, which were performed at a grid size of 96×96×48 and 64×64, respectively. Calculations were performed with a contour length step size of $\Delta s = 0.01$ and a convergence criterion of 10^{-5} as defined by Arora et al. 17 As shown in Figure S10, the free energies were almost degenerate at $\phi_2 = 0.15$ and 0.25. To better resolve the phase behavior at those compositions, we repeated the calculations using a more stringent convergence criterion of 10⁻⁶. Figure S11 shows the results under this stricter convergence criterion, revealing that C15 and HCP phases offer the lowest free energy at low ϕ_2 . Then, we performed grand canonical ensemble calculations between neighboring phases to resolve phase coexistence. Further calculation details can be found elsewhere. 18

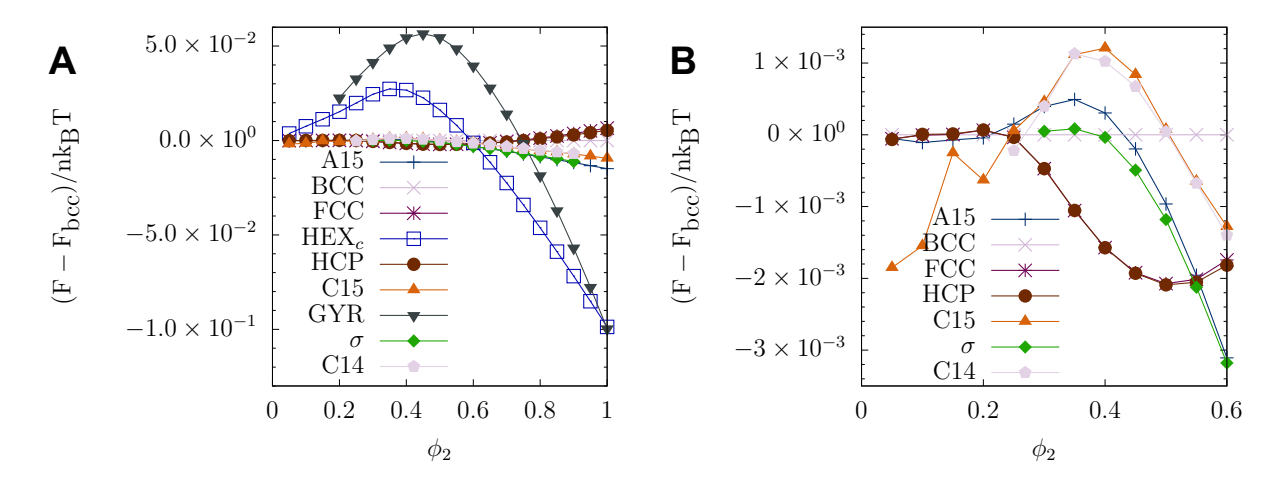


Figure S10. Normalized free energy relative to BCC *versus* ϕ_2 at $\chi N = 28$ for (A) all studied phases and (B) only particle phases.

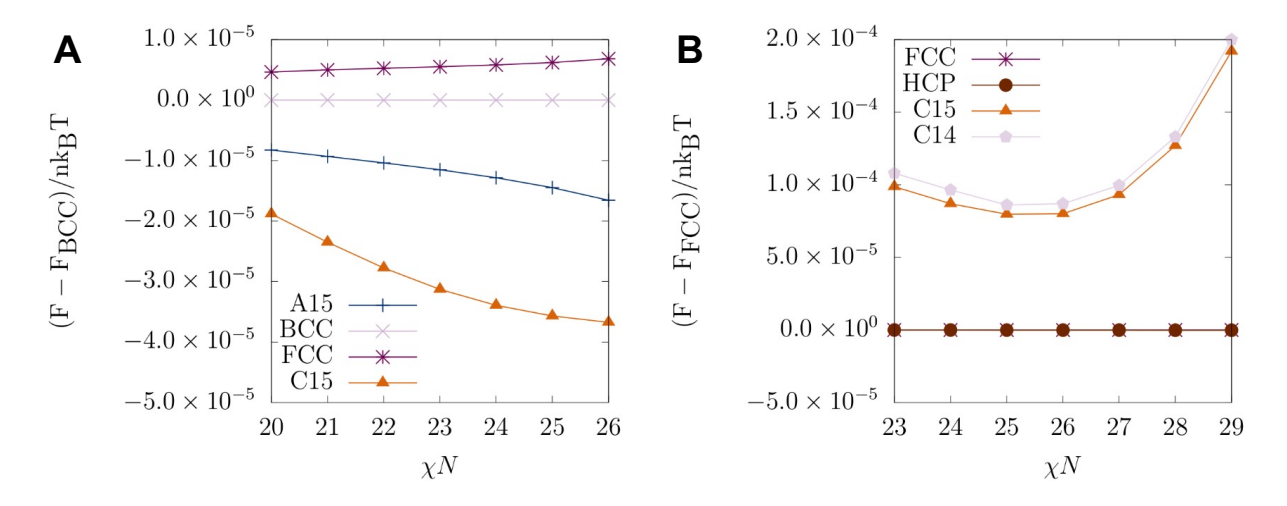


Figure S11. Normalized free energy relative to (A) BCC and (B) FCC *versus* χN at (A) $\phi_2 = 0.15$ and (B) $\phi_2 = 0.25$ for select phases under the more stringent convergence criterion of 10^{-6} .

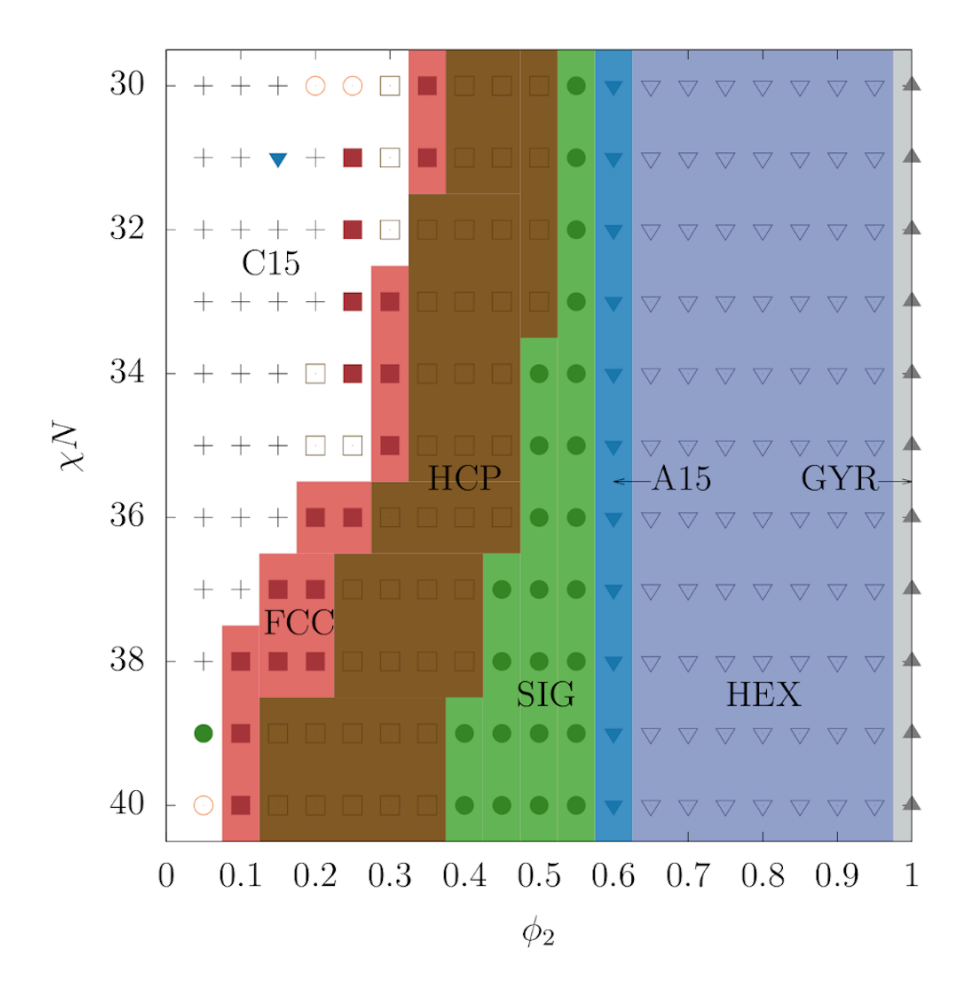


Figure S12. Binary blend phase diagram generated from canonical ensemble SCFT calculations over an extended range of χN ($N_2/N_1 = 1.4$, $N_{S,1} = N_{S,2}$, $f_{B,1} = 0.12$, and $f_{B,2} = 0.38$). Symbols correspond to the double gyroid (gray \blacktriangle), hexagonally-packed cylinder (purple ∇), A15 (blue \blacktriangledown), σ (green \bigcirc), hexagonal close-packed \square), face-centered cubic (red \bigcirc), C14 (orange \circ), and C15 phases (black +).

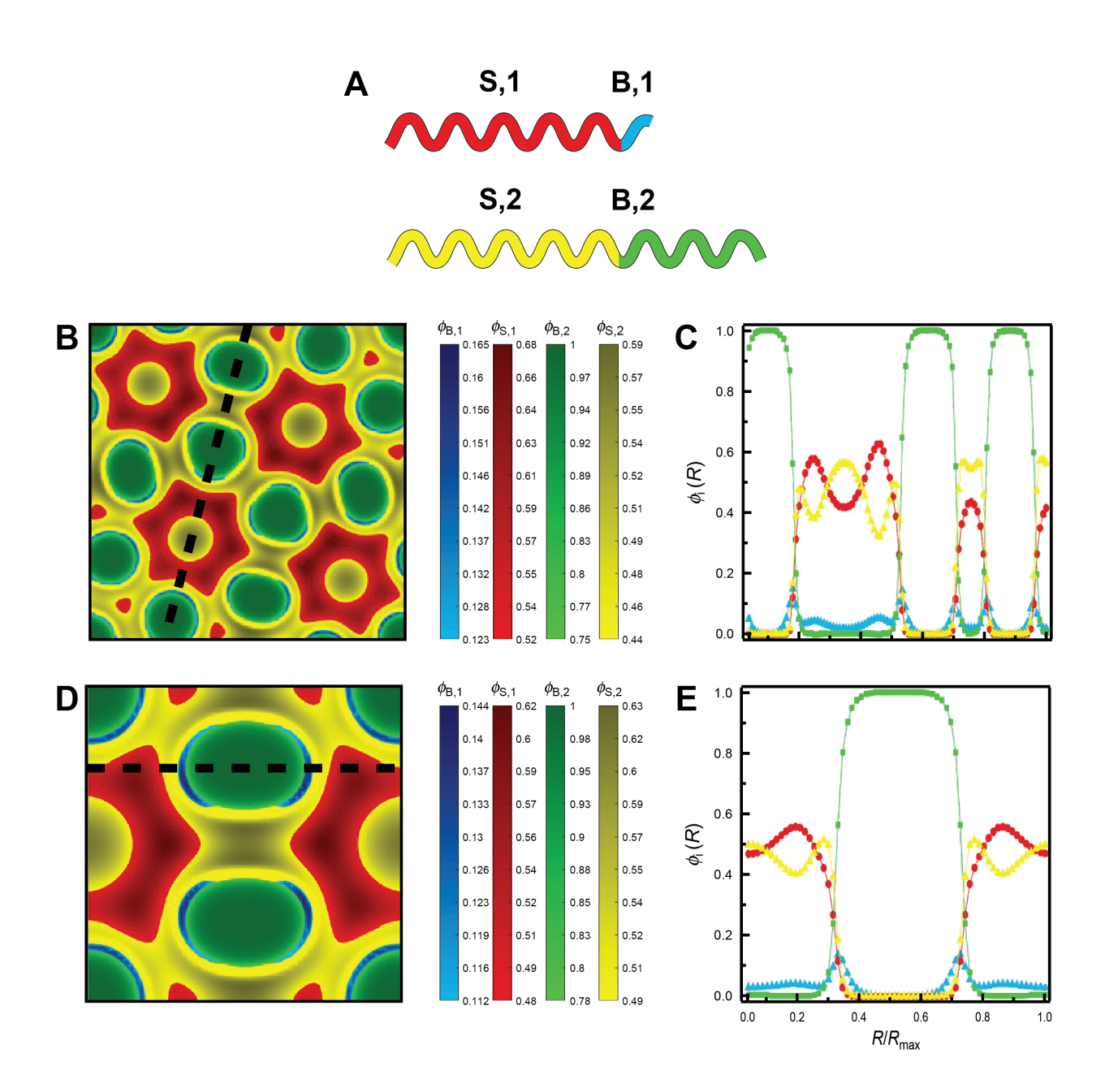


Figure S13. (B,D) Composition maps and (C,E) 1D composition profiles for the (B,C) σ and (D,E) A15 phases in the (001) planes. Data were calculated *via* SCFT for SB3/SB5 blends with (B,C) ϕ_2 = 0.55 and (D,E) 0.60 at $\chi\langle N\rangle$ = 30. ϕ_i is the volume fraction of block i at each position. R/R_{max} is the nondimensional distance along the dashed lines in (B,D), where 0 corresponds to the (C) bottom or (E) left edge of the composition map. The schematic in (A) shows the relative copolymer block lengths. Blue and red shading correspond to the B and S blocks of SB3, whereas green and yellow shading correspond to the B and S blocks of SB5, respectively.

References

- (1) Iwami, S.; Ishimasa, T. Dodecagonal Quasicrystal in Mn-Based Quaternary Alloys Containing Cr, Ni and Si. *Philos. Mag. Lett.* 2015, 95, 229–236. https://doi.org/10.1080/09500839.2015.1038332.
- (2) Lindsay, A. P.; Jayaraman, A.; Peterson, A. J.; Mueller, A. J.; Weigand, S.; Mahanthappa, M. K.; Lodge, T. P.; Bates, F. S. Reevaluation of Poly(Ethylene- Alt -Propylene)- Block Polydimethylsiloxane Phase Behavior Uncovers Topological Close-Packing and Epitaxial Quasicrystal Growth. ACS Nano 2021, ASAP Article. https://doi.org/10.1021/acsnano.1c02420.
- (3) Lindsay, A. P.; Lewis, R. M.; Lee, B.; Peterson, A. J.; Lodge, T. P.; Bates, F. S. A15, σ, and a Quasicrystal: Access to Complex Particle Packings via Bidisperse Diblock Copolymer Blends. ACS Macro Lett. 2020, 9, 197–203. https://doi.org/10.1021/acsmacrolett.9b01026.
- (4) Schmidt, S. C.; Hillmyer, M. A. Morphological Behavior of Model Poly(Ethylene-Alt-Propylene)-b-Polylactide Diblock Copolymers. *J. Polym. Sci. Part B Polym. Phys.* **2002**, 40, 2364–2376. https://doi.org/10.1002/polb.10291.
- (5) Lynd, N. A.; Hillmyer, M. A. Influence of Polydispersity on the Self-Assembly of Diblock Copolymers. *Macromolecules* **2005**, *38*, 8803–8810. https://doi.org/10.1021/ma051025r.
- (6) Cooke, D. M.; Shi, A.-C. Effects of Polydispersity on Phase Behavior of Diblock Copolymers. *Macromolecules* 2006, 39, 6661–6671. https://doi.org/10.1021/ma060717s.
- (7) Lee, S.; Bluemle, M. J.; Bates, F. S. Discovery of a Frank-Kasper σ Phase in Sphere-Forming Block Copolymer Melts. *Science* 2010, 330, 349–353. https://doi.org/10.1126/science.1195552.
- (8) Gillard, T. M.; Lee, S.; Bates, F. S. Dodecagonal Quasicrystalline Order in a Diblock

- Copolymer Melt. *Proc. Natl. Acad. Sci. U. S. A.* **2016**, *113*, 5167–5172. https://doi.org/10.1073/pnas.1601692113.
- Lee, S.; Leighton, C.; Bates, F. S. Sphericity and Symmetry Breaking in the Formation of Frank-Kasper Phases from One Component Materials. *Proc. Natl. Acad. Sci. U. S. A.* 2014, 111, 17723–17731. https://doi.org/10.1073/pnas.1408678111.
- (10) Schulze, M. W.; Lewis, R. M.; Lettow, J. H.; Hickey, R. J.; Gillard, T. M.; Hillmyer, M. A.; Bates, F. S. Conformational Asymmetry and Quasicrystal Approximants in Linear Diblock Copolymers. *Phys. Rev. Lett.* 2017, *118*, 207801. https://doi.org/10.1103/PhysRevLett.118.207801.
- (11) Kim, K.; Arora, A.; Lewis, R. M.; Liu, M.; Li, W.; Shi, A. C.; Dorfman, K. D.; Bates, F. S. Origins of Low-Symmetry Phases in Asymmetric Diblock Copolymer Melts. *Proc. Natl. Acad. Sci. U. S. A.* 2018, *115*, 847–854. https://doi.org/10.1073/pnas.1717850115.
- (12) Kim, K.; Schulze, M. W.; Arora, A.; Lewis, R. M.; Hillmyer, M. A.; Dorfman, K. D.; Bates, F. S. Thermal Processing of Diblock Copolymer Melts Mimics Metallurgy. *Science* 2017, 356, 520–523. https://doi.org/10.1126/science.aam7212.
- (13) Hiemenz, P. C.; Lodge, T. P. *Polymer Chemistry*, 2nd Editio.; CRC Press: Boca Raton, 2007.
- (14) Dechy-Cabaret, O.; Martin-Vaca, B.; Bourissou, D. Controlled Ring-Opening Polymerization of Lactide and Glycolide. *Chem. Rev.* 2004, 104, 6147–6176. https://doi.org/10.1021/CR040002S.
- (15) Schmidt, S. C.; Hillmyer, M. A. Synthesis and Characterization of Model Polyisoprene–Polylactide Diblock Copolymers. *Macromolecules* 1999, 32, 4794–4801. https://doi.org/10.1021/MA9900277.

- (16) Arora, A.; Qin, J.; Morse, D. C.; Delaney, K. T.; Fredrickson, G. H.; Bates, F. S.; Dorfman, K. D. Broadly Accessible Self-Consistent Field Theory for Block Polymer Materials Discovery. *Macromolecules* 2016, 49, 4675–4690. https://doi.org/10.1021/acs.macromol.6b00107.
- (17) Arora, A.; Morse, D. C.; Bates, F. S.; Dorfman, K. D. Accelerating Self-Consistent Field Theory of Block Polymers in a Variable Unit Cell. *J. Chem. Phys.* 2017, 146, 244902. https://doi.org/10.1063/1.4986643.
- (18) Liu, M.; Qiang, Y.; Li, W.; Qiu, F.; Shi, A. C. Stabilizing the Frank-Kasper Phases via Binary Blends of AB Diblock Copolymers. *ACS Macro Lett.* **2016**, *5*, 1167–1171. https://doi.org/10.1021/acsmacrolett.6b00685.